Journal of Building Engineering 73 (2023) 106738

Contents lists available at ScienceDirect

Journal of Building Engineering

journal homepage: www.elsevier.com/locate/jobe

Full length article

A multi-temporal DInSAR-based method for the assessment of the 3D rigid motion of buildings and corresponding uncertainties

Elisa Bassoli, Loris Vincenzi *, Francesca Grassi, Francesco Mancini

University of Modena and Reggio Emilia, Department of Engineering "Enzo Ferrari", Modena, Italy

ARTICLE INFO

Keywords:
Multi-temporal DInSAR
Persistent scatterer interferometry
Structural monitoring
3D rigid motion
Motion parameter uncertainty

ABSTRACT

This paper investigates the performances of the multi-temporal DInSAR technique for the structural monitoring of single buildings. The application of the multi-temporal DInSAR technique at building or infrastructure scale is enabled by the high imaging capability of the current generation of SAR constellations. Within this framework, the paper proposes an analytical procedure for the reconstruction of the 3D rigid motion of single buildings based on SAR measurements. To successfully reconstruct the structural displacement, measurements from dual orbits are required by the method. The proposed procedure is tested through numerical analyses accounting for uncertainties affecting SAR data, both in the displacement measurements and in the positioning of the main persistent scatterers. Numerical simulation results allow for the quantification of uncertainties in the estimation of the motion parameters. An analytical model is also proposed to estimate the motion parameter uncertainties depending only on the building geometry, the satellite orbit inclinations and the number of persistent scatterers, with no need to know their exact positions. The main benefit of the proposed analytical model is that it can be adopted in real applications to a priori evaluate the precision by which the motion components can be estimated in order to assess the reliability of the structural monitoring based on SAR interferometry. A very good match between numerical and analytical motion parameter uncertainties is achieved. Finally, the proposed method to reconstruct the 3D rigid motion and assess the corresponding uncertainties is applied to a real case study in Rome (Italy).

1. Introduction

Preventive conservation and maintenance of the existing built heritage against structural deterioration is a key aspect for modern societies [1]. In this context, measurement and monitoring activities are the basis for structural health assessment [2,3]. Over the past few years, remote sensing techniques, such as multi-temporal Differential Interferometric Synthetic Aperture Radar (DInSAR), have gained increasing attention in the field of structural health monitoring thanks to the recent development of satellites and constellations based on X-band SAR systems (e.g., COSMO-SkyMed, TerraSAR-X/TanDEM-X) with advanced capabilities in terms of revisit time and meter-level spatial resolution. Besides, the multi-temporal DInSAR methodology has proven its ability to provide displacement measurements with millimetric precision [4–7]. Although the DInSAR technique has been used since from the late 80 s to study large scale displacements (such a subsidence, landslides, earthquakes, volcanic phenomena and polar caps) [8–10], only the imaging capability of the current generation of SAR constellations allowed for applications at building or infrastructure scale. Indeed, the ability of the mentioned satellites and constellations to provide data with meter to sub-meter spatial resolution allows

* Corresponding author.
E-mail address: loris.vincenzi@unimore.it (L. Vincenzi).

https://doi.org/10.1016/j.jobe.2023.106738
Received 8 November 2022; Received in revised form 31 March 2023; Accepted 1 May 2023
Available online 5 May 2023

measuring displacements of several points over the single structure with millimetric precision and paved the way to successive analyses oriented to the structural monitoring based on multi-temporal DInSAR.

Among these, applications of satellite radar interferometry to the assessment of building structural damage induced by ground deformations and slope failure have been reported by [11–15]. Furthermore, the authors proposed an approach based on the combination of multi-temporal DInSAR and GIS dataset to investigate and separate several contributions to subsidence phenomena, such as the consolidation processes after building construction [16]. About the issue of structural health monitoring with radar satellite data, Cavalagli et al. [4] reported an investigation on static monitoring of historical monuments complemented by in-situ measurements and Gernhardt and Bamler [17] introduced the potentialities of meter-resolution SAR data in the deformation monitoring of single buildings. More recently Talledo et al. [18] explored the potential and limitations of satellite data for structural assessment and monitoring and Di Carlo et al. [19] investigated the use of multi-temporal DInSAR products and historical surveys data for buildings structural monitoring. In addition, some applications oriented to the monitoring of infrastructures have been also proposed in [20–22].

However, several aspects related to the use of multi-temporal DInSAR techniques to monitor single structures remain challenging. In particular, the reliability of structural monitoring based on radar satellite data needs to be carefully assessed due to the very small displacements characterizing a structural motion. Moreover, displacements of persistent scatterers (PSs) obtained from multi-temporal DInSAR on a target building need to be combined to reconstruct the effective structural motion, taking into account the unavoidable displacement measurement uncertainties and the errors in the positioning of the scatterers. However, to fully exploit the redundancy of measurements provided by the multi-temporal DInSAR method at building scale, some spatial and temporal resampling of PSs available from the processing of dual orbits may be required [18]. A typical drawback of standard interpolation procedures is that they are usually designed with the main purpose of fitting SAR measurements as better as possible, neglecting the high uncertainty that may affect the PS positions. This may cause an overfitting of data or even a fitting of the measurement noise. The reconstruction of the global building displacement becomes more straightforward when the building can be considered as a rigid body. This happens, for instance, when dealing with buildings suffering from foundation settlements that cause a rigid motion of the structure. In this case, the hypothesis of rigid motion allows to easily relate the PS displacements to evaluate the global behaviour. Also in this case, however, the ability to reconstruct the 3D rigid motion of a building requires a careful analysis about the impact of uncertainties on slant-oriented displacements and positioning errors of the scatterers. These uncertainties cause inaccuracies in the evaluation of the rigid motion that need to be investigated to assess the reliability of SAR Interferometry for structural monitoring. A comprehensive analysis about the uncertainties affecting the multi-temporal DInSAR displacements and their propagation to the derived rigid motion of buildings is not available in the recent literature. It could inform about the minimal precision required to the multi-temporal DInSAR products (in terms of measures, positions and number of PSs) used in the structural analysis to detect a particular deformation phenomenon.

To cover this gap, the present paper proposes a method for the evaluation of isolated buildings displacements from satellite SAR measurements. This method aims at assessing displacements related to the rigid motion of buildings, generally caused by foundation settlements. These can be due to structural weaknesses, underground water or gas extraction/injection activities and close presence of construction sites. In particular, the method is focused on the relative motion of isolated buildings with respect to the surroundings, which may result in damage to structural and non-structural elements. The building rigid motion includes vertical settlements (i.e. vertical rigid displacements) and rigid rotations. Although vertical settlements typically do not affect the structural stress state, they can cause problems with the services entering the structure (e.g. water and gas pipes) and accessibility issues. Moreover, the higher the values of vertical settlement, the higher the probability of differential settlements. Unlike vertical settlements, differential settlements and rigid rotations can cause additional stress state that can compromise the structural integrity. Rigid rotations can also limit the functionality of elevators especially in high-rise buildings. For these reasons, several researchers have proposed, on a statistical basis, limit values for the foundation movements and differential settlements depending on the type of structure or infrastructure. As an example, these limits can be found in [23,24].

The rigid motion of a building is reconstructed starting from displacements along the line of sight (LOS) direction detected by persistent scatterer interferometry (PSI) techniques. To enable insights into building displacements, LOS measurements from dual orbits and high resolution data are required by the model. Due to the limited sensitivity of the SAR measurements to displacements in north–south direction, the reconstruction of the original motion vector is limited to the three rotations and displacement components in west–east and vertical directions [4,17,25]. The method to reconstruct the building displacements proposed in this paper applies for every isolated building or a portion of it moving like a rigid body.

To evaluate the reliability of the identified structural motion, this paper also proposes an analytical method for quantifying the uncertainties affecting the estimated motion parameters. Expressions of the uncertainties presented in this paper are achieved considering the same height for all of the identified PSs, that is the case of buildings with flat roofs. However, the same expressions can be generalized, at the expense of their simpleness, to account for different PS heights, whatever they might be. The main benefit of the proposed analytical expressions is that they can be adopted in real applications to evaluate the estimation precision of the rigid motion parameters depending only on the number of potentially identified PSs, the building geometry and the satellite orbit inclinations, with no need to know the exact positions of the PSs.

The paper is organized as follows. The procedure to evaluate the 3D rigid motion components starting from satellite measurements is presented in Section 2. Section 3 shows the numerical analyses performed to test the procedure of Section 2 based on the simulation of the satellite measurements accounting for measurement and positioning uncertainties. Monte Carlo analyses are performed to assess the uncertainties of the estimated motion parameters. Analytical expressions of the estimated parameter uncertainties are derived in Section 4 and compared to the numerical ones. Finally, Section 6 presents the results of a real case study placed in Rome (Italy) in terms of identified rigid motion parameters and corresponding uncertainties.

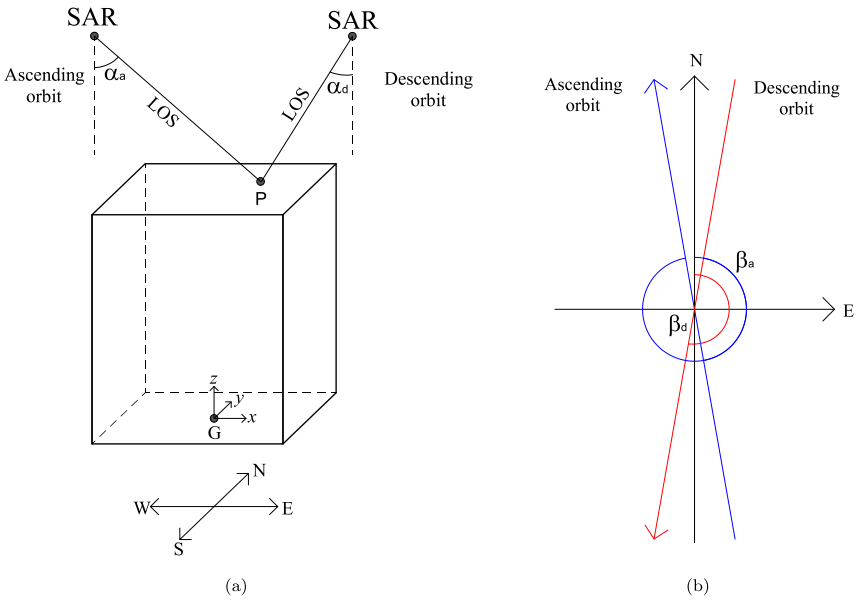

Fig. 1. Coordinate system and imaging geometries of the ascending and descending orbit.

2. Evaluation of the 3D rigid motion

This section outlines the procedure to evaluate the rigid motion of an isolated building starting from SAR measurements. The procedure relies on the combination of measurements acquired from ascending and descending satellite orbits. SAR data acquired from the two satellite acquisition geometries are temporally and spatially independent [25], meaning that the displacements of PSs measured from the two satellite acquisition geometries are measured at different acquisition times and in different positions. Thanks to the hypothesis of rigid motion, PS displacements measured from the ascending and descending orbit can be analysed together with no need for geometrical interpolation, i.e. it is not necessary that the PS measured from the two orbits are co-located. Also the temporal correlation is not required as the structural monitoring relies on mean annual displacement values. On the contrary, data measured from the two satellite geometries need to be properly temporally realigned when investigating the building behaviour at a specific time [18].

Let us consider the reference system shown in Fig. 1, where x, y and z represent, respectively, the west–east, north–south and vertical direction. Assuming clockwise rotations as positive, the displacement of a generic point P relative to G, namely the point on the ground corresponding to the centre of gravity, is expressed as:

$$\begin{cases} v_{x,\mathrm{P}} = v_{x,\mathrm{G}} + \Phi_{y,\mathrm{G}}\, D_{z,\mathrm{P}} - \Phi_{z,\mathrm{G}}\, D_{y,\mathrm{P}} \\ v_{y,\mathrm{P}} = v_{y,\mathrm{G}} - \Phi_{x,\mathrm{G}}\, D_{z,\mathrm{P}} + \Phi_{z,\mathrm{G}}\, D_{x,\mathrm{P}} \\ v_{z,\mathrm{P}} = v_{z,\mathrm{G}} + \Phi_{x,\mathrm{G}}\, D_{y,\mathrm{P}} - \Phi_{y,\mathrm{G}}\, D_{x,\mathrm{P}} \end{cases} \tag{1}$$

being $v_{x,\mathrm{G}}$, $v_{y,\mathrm{G}}$ and $v_{z,\mathrm{G}}$ the displacements in the three directions and $\Phi_{x,\mathrm{G}}$, $\Phi_{y,\mathrm{G}}$ and $\Phi_{z,\mathrm{G}}$ the rotation around the three axes. Finally, $D_{x,\mathrm{P}}$, $D_{y,\mathrm{P}}$ and $D_{z,\mathrm{P}}$ are the distances between P and G in x, y and z direction, respectively.

The displacement measured on the generic point P of the building along the LOS direction of the ascending and descending satellite orbit, i.e. $d_{a,P}$ and $d_{d,P}$, can be written as a function of the displacement components of the same point:

$$\begin{cases} d_{a,P} = (-v_{x,\mathrm{P}} \cos\beta_a + v_{y,\mathrm{P}} \sin\beta_a) \sin\alpha_a + v_{z,\mathrm{P}} \cos\alpha_a \\ d_{d,P} = (-v_{x,\mathrm{P}} \cos\beta_d + v_{y,\mathrm{P}} \sin\beta_d) \sin\alpha_d + v_{z,\mathrm{P}} \cos\alpha_d \end{cases} \tag{2}$$

where α_a and α_d are the incidence angles of the ascending and descending satellite orbit, respectively (see Fig. 1(a)), while β_a and β_d are the heading angles of the satellite orbits (see Fig. 1(b)). Typical values of the heading angles are such that $\sin\beta$ and $\cos\beta$ can be approximated to 0 and ± 1, respectively (in particular $\beta_a = 350°$ and $\beta_d = 190°$ for COSMO-SkyMed). In this case, Eq. (2) becomes:

$$\begin{cases} d_{a,P} = -v_{x,\mathrm{P}} \sin\alpha_a + v_{z,\mathrm{P}} \cos\alpha_a \\ d_{d,P} = v_{x,\mathrm{P}} \sin\alpha_d + v_{z,\mathrm{P}} \cos\alpha_d \end{cases} \tag{3}$$

This means that the limited sensitivity of the SAR to displacements in the north–south direction (namely the y direction) allows for a reliable estimation of the following rigid motion components: $v_{x,\mathrm{G}}$, $v_{z,\mathrm{G}}$, $\Phi_{x,\mathrm{G}}$, $\Phi_{y,\mathrm{G}}$ and $\Phi_{z,\mathrm{G}}$.

By substituting Eq. (1) into Eq. (3), Eq. (3) can be written in the following matrix form:

$$\begin{bmatrix} d_{a,\mathrm{P}} \\ d_{d,\mathrm{P}} \end{bmatrix} = \begin{bmatrix} -\sin\alpha_a & \cos\alpha_a & D_{y,\mathrm{P}}\cos\alpha_a & (-D_{z,\mathrm{P}}\sin\alpha_a - D_{x,\mathrm{P}}\cos\alpha_a) & D_{y,\mathrm{P}}\sin\alpha_a \\ \sin\alpha_d & \cos\alpha_d & D_{y,\mathrm{P}}\cos\alpha_d & (D_{z,\mathrm{P}}\sin\alpha_d - D_{x,\mathrm{P}}\cos\alpha_d) & -D_{y,\mathrm{P}}\sin\alpha_a \end{bmatrix} \begin{bmatrix} v_{x,\mathrm{G}} \\ v_{z,\mathrm{G}} \\ \Phi_{x,\mathrm{G}} \\ \Phi_{y,\mathrm{G}} \\ \Phi_{z,\mathrm{G}} \end{bmatrix} \tag{4}$$

The rigid motion components $v_{x,\mathrm{G}}$, $v_{z,\mathrm{G}}$, $\Phi_{x,\mathrm{G}}$, $\Phi_{y,\mathrm{G}}$ and $\Phi_{z,\mathrm{G}}$ can be determined only if enough displacement measurements are available. Considering N_S measurements, n for the ascending orbit and m for the descending orbit, Eq. (4) becomes:

$$\begin{bmatrix} d_{a,1} \\ \vdots \\ d_{a,n} \\ d_{d,1} \\ \vdots \\ d_{d,m} \end{bmatrix} = \begin{bmatrix} -\sin\alpha_a & \cos\alpha_a & D_{ya,1}\cos\alpha_a & (-D_{za,1}\sin\alpha_a - D_{xa,1}\cos\alpha_a) & D_{ya,1}\sin\alpha_a \\ \vdots & \vdots & \vdots & \vdots & \vdots \\ -\sin\alpha_a & \cos\alpha_a & D_{ya,n}\cos\alpha_a & (-D_{za,n}\sin\alpha_a - D_{xa,n}\cos\alpha_a) & D_{ya,n}\sin\alpha_a \\ \sin\alpha_d & \cos\alpha_d & D_{yd,1}\cos\alpha_d & (D_{zd,1}\sin\alpha_d - D_{xd,1}\cos\alpha_d) & -D_{yd,1}\sin\alpha_a \\ \vdots & \vdots & \vdots & \vdots & \vdots \\ \sin\alpha_d & \cos\alpha_d & D_{yd,m}\cos\alpha_d & (D_{zd,m}\sin\alpha_d - D_{xd,m}\cos\alpha_d) & -D_{yd,m}\sin\alpha_a \end{bmatrix} \begin{bmatrix} v_{x,\mathrm{G}} \\ v_{z,\mathrm{G}} \\ \Phi_{x,\mathrm{G}} \\ \Phi_{y,\mathrm{G}} \\ \Phi_{z,\mathrm{G}} \end{bmatrix} \tag{5}$$

with $N_S = n+m$. $D_{xa,i}$, with $i = 1,..n$, denotes the distance in x direction between the ith PS identified from the ascending orbit and G, while $D_{xd,j}$, with $j = 1,..m$, is the distance between the jth PS of the descending orbit and G. The same goes for the distances in y and z direction. Eq. (5) can be synthetically presented as:

$$\mathbf{M} = \mathbf{S}\,\boldsymbol{\theta} \tag{6}$$

where

$$\mathbf{M} = \begin{bmatrix} d_{a,1} \\ \vdots \\ d_{a,n} \\ d_{d,1} \\ \vdots \\ d_{d,m} \end{bmatrix}; \quad \boldsymbol{\theta} = \begin{bmatrix} v_{x,\mathrm{G}} \\ v_{z,\mathrm{G}} \\ \Phi_{x,\mathrm{G}} \\ \Phi_{y,\mathrm{G}} \\ \Phi_{z,\mathrm{G}} \end{bmatrix} \tag{7}$$

$$\mathbf{S} = \begin{bmatrix} -\sin\alpha_a & \cos\alpha_a & D_{y,1}\cos\alpha_a & (-D_{z,1}\sin\alpha_a - D_{x,1}\cos\alpha_a) & D_{y,1}\sin\alpha_a \\ \vdots & \vdots & \vdots & \vdots & \vdots \\ -\sin\alpha_a & \cos\alpha_a & D_{y,n}\cos\alpha_a & (-D_{z,n}\sin\alpha_a - D_{x,n}\cos\alpha_a) & D_{y,n}\sin\alpha_a \\ \sin\alpha_d & \cos\alpha_d & D_{y,1}\cos\alpha_d & (D_{z,1}\sin\alpha_d - D_{x,1}\cos\alpha_d) & -D_{y,1}\sin\alpha_a \\ \vdots & \vdots & \vdots & \vdots & \vdots \\ \sin\alpha_d & \cos\alpha_d & D_{y,m}\cos\alpha_d & (D_{z,m}\sin\alpha_d - D_{x,m}\cos\alpha_d) & -D_{y,m}\sin\alpha_a \end{bmatrix} \tag{8}$$

with $\mathbf{M}$ the N_S-by-1 vector collecting the displacements and $\mathbf{S}$ a N_S-by-5 matrix whose terms depend on the positions of the PS and the incidence angles of the two satellite acquisition geometries. Finally, $\boldsymbol{\theta}$ is the vector that contains the five motion parameters. Note that the numerosity and locations of PSs identified from the ascending and descending orbit and listed in Eq. (8) generally do not coincide.

It is important to highlight that, due to measurement and positioning uncertainties, measured displacements $\mathbf{M}*$ are not exactly equal to modelled displacements $\mathbf{M} = \mathbf{S}\,\boldsymbol{\theta}$. Optimal values of the motion parameters $\boldsymbol{\theta}$ that minimize the difference between modelled $\mathbf{M}$ and measured $\mathbf{M}*$ displacements are estimated through the least square method as [26]:

$$\hat{\boldsymbol{\theta}} = (\mathbf{S}^{\mathrm{T}}\mathbf{S})^{-1}\mathbf{S}^{\mathrm{T}}\mathbf{M}* \tag{9}$$

In order to compute the rigid movements that best approximate the available measurements, the number of observations N_S must be significantly higher than the unknown parameters, namely the rigid motion components gathered in $\boldsymbol{\theta}$.

To evaluate the relative displacement of the building with respect to the ground, the same procedure has to be applied with reference to the persistent scatterers on the ground. The relative rigid motion of the building is then estimated as the difference between the rigid motion obtained from the PSs on the building and those of the ground. This approach allows to distinguish the displacement of the ground from that of the building. PSs on the building are distinguished from those of the ground thanks to their height that can be estimated according to [5,27,28].

Finally, the hypothesis of rigid motion needs to be verified. To this purpose, different subsets of the N_S PSs belonging to the building are created and the rigid motion components evaluated for each subset according to Eq. (9). A low variability of the rigid motion components identified from the different subsets proves the reliability of the assumption.

3. Numerical simulations

This section presents numerical analyses designed to evaluate the performances of the procedure outlined in Section 2. Analyses are based on (i) the imposition of rigid motion to hypothetical buildings, (ii) simulation of the satellite measurements including measurement and positioning uncertainties, (iii) evaluation of the rigid motion according to Section 2, (iv) comparison between imposed and estimated displacements and (v) assessment of the variability of results. A key aspect of the presented analyses lies

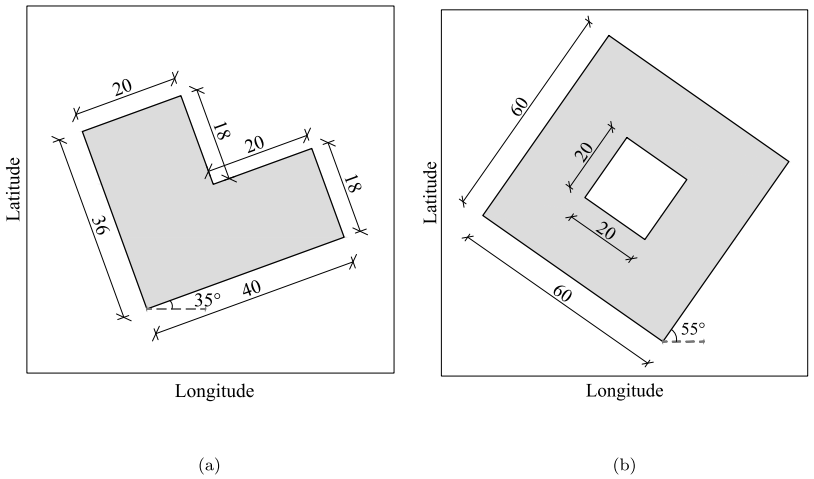

Fig. 2. Plan view of the two case studies: (a) L-shaped building and (b) square building with a inner yard. Dimensions are in meters.

Table 1
Ranges of variation of the imposed motion parameters.

		$v_{x,G}$ [mm/yr]	$v_{z,G}$ [mm/yr]	$\Phi_{x,G}$ [mrad/yr]	$\Phi_{y,G}$ [mrad/yr]	$\Phi_{z,G}$ [mrad/yr]
Group 1	min	0	0	–	0	0
	max	15	75	–	75	1.5
	step	0.5	2.5	–	2.5	0.05
Group 2	min	–	0	0	–	–
	max	–	75	3	–	–
	step	–	2.5	0.1	–	–

in the simulation of the satellite measurements. Besides the projection of each imposed motion component into the satellite line of sight, all the uncertainties affecting SAR data have to be introduced. These uncertainties are related to inaccuracies both in the PS displacement measurements and positioning, as detailed in Section 3.2. Note that the PS displacement along the LOS is not actually "measured" but it is numerically simulated. Nevertheless, for the sake of simplicity, we use "measurement uncertainties" to indicate uncertainties related to the PS displacement along the LOS. The analysed numerical case studies are introduced in Section 3.1, while results and main findings of the numerical simulations are presented in Sections 3.3 and 3.4, respectively.

3.1. Numerical case studies

The two numerical case studies shown in Fig. 2 are investigated. The first one is a building presenting a L-shaped plan and a flat roof, inclined by 20° relative to west–east and 15 m high. The second case study is a 28 m high building with a square plan and an inner yard, inclined by 55° relative to west–east. In both cases, the incidence angles of the two satellite orbits are assumed equal to 30° and 25° for the ascending and descending orbit, respectively (namely $\alpha_a = 30°$ and $\alpha_d = 25°$). Two different groups of simulations are performed, differing in the imposed rigid motion displacements, namely $v_{x,G}$, $v_{z,G}$, $\Phi_{y,G}$ and $\Phi_{z,G}$ in one case and $v_{z,G}$ and $\Phi_{x,G}$ in the other one. Several analysis sets are defined in terms of building shape (L-shaped or square), number of PS of the ascending ($n = 60$ or 30) and descending ($m = 40$ or 70) orbit and imposed rigid motion displacements varying according to the ranges of Table 1, where "mrad" denotes milliradians.

3.2. Positioning and measurements uncertainties

Satellite measurements are simulated by adding measurement and positioning uncertainties to the motion components projected along the satellite LOS. Positioning uncertainties analysed in the following are related to the position in plan of the PSs as it assumed that the height of the building is known thanks to a geometrical survey, and thus the PS vertical positions. The reader is referred to Section 4.4 for a detailed discussion about the vertical positioning uncertainty. For each simulation, the difference between the imposed motion parameters and the estimated ones allows to quantify the effect of the measurement and/or positioning uncertainties. Assuming to deal with COSMO-SkyMed data, which are particularly suitable for applications at building or infrastructure scale, the typical displacement precision $\overline{\sigma}_M$ is considered as about 1 or 2 mm/yr. However, analyses with displacement precision up to 5 mm/yr are also performed in order to investigate its effect on the results.

Aiming at characterizing the variability of results related to measurement uncertainties, Monte Carlo simulations are carried out for each analysis set by randomly extracting N_S persistent scatterers on the building and adding a random noise to each measure.

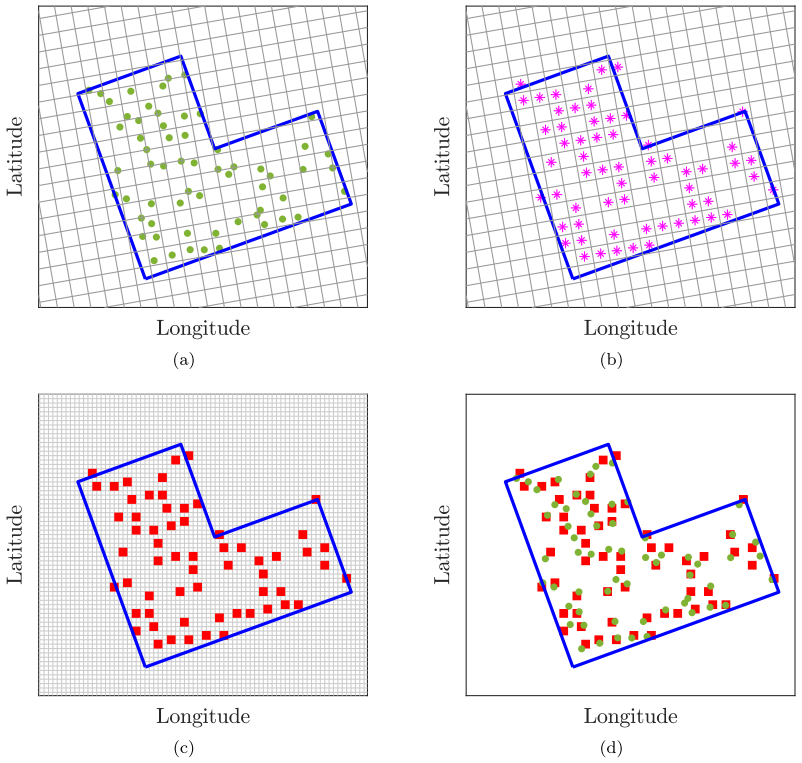

Fig. 3. Example of PSs measured from the ascending orbit with $n = 60$: (a) exact position (green markers •), (b) PS located in the 3 m × 3 m grid cell centres (magenta markers ∗), (c) positions of PSs after the truncation of the coordinates to the fifth digital place (red markers ■) and (d) comparison between the actual (green markers •) and the processed (red markers ■) PS positions. (For interpretation of the references to colour in this figure legend, the reader is referred to the web version of this article.)

The noise is randomly extracted from a normal distribution with standard deviation $\overline{\sigma}_M$. As far as uncertainties in the PS positioning are concerned, these are related to the characteristic spatial resolution of SAR images which does not allow for the knowledge of the exact position of the PS. COSMO-SkyMed data present a ground range geometric resolution and an azimuth geometric resolution of 3 m. This means that the investigated area is ideally divided into a grid of 3 m × 3 m and at most one PS can be identified in each grid cell. Indeed, there is no guarantee that a PS is measured in each grid cell. To account for this source of uncertainty, others Monte Carlo simulations are performed for each analysis set. In this case, the procedure outlined in the following is employed to estimate the positions of the PS starting from the actual one, which is obviously unknown in real applications. Finally, others Monte Carlo simulations are performed considering the contribution of both measurement and positioning uncertainties.

With reference to the numerical case study of a L-shaped building, Fig. 3(a) shows the resolution grid of the ascending orbit, inclined by 350° relative to north–south, and an example of measured PSs with $n = 60$. In real applications, the main scatterer of a grid cell can be located anywhere depending on the reflectivity of the points belonging to the cell. Depending on the adopted PSI procedure, the PS annual displacement can be attribute to the cell centre (see, for instance, [29]) or a sub-pixel correction of the PS position can be performed (such as [30,31]). PSI procedures that attribute the PS annual displacement to the cell centre are more common when dealing with high resolution data, as for structural monitoring applications. For this reason, we assume that the main scatterer is located in a random position inside the grid cell and the corresponding displacement is assigned to the cell centre, as represented in Fig. 3(b). Moreover, as the ground range-azimuth grid is inclined with respect to the geographic coordinate grid, PS positions need to be resampled to the geographic coordinate grid. Spatial resampling operation must be such as to avoid aliasing during regridding involving a rotation factor [25]. To this aim, the PS coordinates (in terms of latitude and longitude) are truncated to the fifth digital place, corresponding to a resolution of 0.8 m. This is represented in Fig. 3(c). To sum up, Fig. 3(d) compares the exact and the processed positions of the PSs. Being the exact positions of PSs unknown, the displacements of the green dots in Fig. 3(a) are attributed to the red squares of Fig. 3(d), introducing unavoidable uncertainties. The high number of performed numerical analyses allows to statistically characterize the distance between the exact and the processed position of persistent scatterers. This distance presents a distribution resembling a Gaussian distribution, with values in the range $[-1.90; 1.90]$ m mainly concentrated close to 0 m. Indeed, the distance between the exact and the processed position of the PS cannot be greater than 1.90 m, otherwise the PS would be part of a different grid cell. This distribution is modelled as a Gaussian-like distribution with a standard deviation of 0.90 m ($\overline{\sigma}_P = 0.90$ m). The so-defined distribution can be adopted for every building shape when dealing with COSMO-SkyMed data. The same procedure is repeated considering grid cells of different dimensions, namely 1 m × 1 m, 2 m × 2 m,

Table 2
Simulation parameters and statistics of the estimated displacements for two analysis sets: Case A and Case B. θ_{imp}= imposed value of the motion component, $\mu(\theta_r)$, $\sigma(\theta_r)$, CoV(θ_r) = mean value, standard deviation and coefficient of variation of the estimated motion component.

		Case A				Case B			
Building		L-shaped				Square			
n	[–]	60				30			
m	[–]	40				70			
$\overline{\sigma}_M$	[mm/yr]	1				2			
Grid cell	[m]	3 × 3				3 × 3			
Simulations	[–]	3000				3000			
Measurement unc.		$\theta_{r,\text{imp}}$	$\mu(\theta_r)$	$\sigma(\theta_r)$	CoV(θ_r)	$\theta_{r,\text{imp}}$	$\mu(\theta_r)$	$\sigma(\theta_r)$	CoV(θ_r)
$v_{x,G}$	[mm/yr]	10	10.0035	0.538	5.38%	0	−0.0003	0.303	–
$v_{z,G}$	[mm/yr]	50	49.9970	0.234	0.47%	50	50.0012	0.122	0.24%
$\Phi_{x,G}$	[mrad/yr]	0	0.0004	0.028	–	2	2.0000	0.007.	0.34%
$\Phi_{y,G}$	[mrad/yr]	2	1.9996	0.020	0.99%	0	0.0001	0.006	–
$\Phi_{z,G}$	[mrad/yr]	1	0.9997	0.051	5.06%	0	−0.0001	0.014	–
Positioning unc.		$\theta_{r,\text{imp}}$	$\mu(\theta_r)$	$\sigma(\theta_r)$	CoV(θ_r)	$\theta_{r,\text{imp}}$	$\mu(\theta_r)$	$\sigma(\theta_r)$	CoV(θ_r)
$v_{x,G}$	[mm/yr]	10	10.2236	0.432	4.22%	0	−0.1829	0.484	–
$v_{z,G}$	[mm/yr]	50	50.0365	0.214	0.43%	50	50.0145	0.199	0.40%
$\Phi_{x,G}$	[mrad/yr]	0	0.0224	0.025	–	2	1.9946	0.011	0.54%
$\Phi_{y,G}$	[mrad/yr]	2	1.9855	0.014	0.72%	0	0.0052	0.009	–
$\Phi_{z,G}$	[mrad/yr]	1	0.9915	0.043	4.33%	0	−0.0002	0.022	–
Measurement and positioning unc.		$\theta_{r,\text{imp}}$	$\mu(\theta_r)$	$\sigma(\theta_r)$	CoV(θ_r)	$\theta_{r,\text{imp}}$	$\mu(\theta_r)$	$\sigma(\theta_r)$	CoV(θ_r)
$v_{x,G}$	[mm/yr]	10	10.2270	0.691	6.75%	0	−0.1832	0.569	–
$v_{z,G}$	[mm/yr]	50	50.0334	0.316	0.63%	50	50.0157	0.233	0.47%
$\Phi_{x,G}$	[mrad/yr]	0	0.0228	0.037	–	2	1.9946	0.016	0.63%
$\Phi_{y,G}$	[mrad/yr]	2	1.9851	0.024	1.22%	0	0.0051	0.011	–
$\Phi_{z,G}$	[mrad/yr]	1	0.9913	0.066	6.63%	0	−0.0002	0.026	–

4 m × 4 m and 5 m × 5 m, that may characterize SAR systems different from COSMO-SkyMed. In those cases, the positioning precision $\overline{\sigma}_P$ results 0.38 m for the grid 1 m × 1 m, 0.61 m for the grid 2 m × 2 m, 1.22 m for the grid 4 m × 4 m and 1.47 m for the grid 5 m × 5 m.

3.3. Results

Let us now analyse in detail the results obtained for two analysis sets referred to as "Case A" and "Case B". Parameters of the two sets are listed in Table 2 together with the imposed values of motion parameters $\theta_{r,\text{imp}}$ and the mean values $\mu(\theta_r)$, standard deviations $\sigma(\theta_r)$ and coefficients of variation CoV(θ_r) of the estimated displacements. Note that θ_r generally indicates the rth motion parameter gathered in $\boldsymbol{\theta}$. Coefficients of variation are calculated for non-zero imposed displacements only.

Table 2 compares the results obtained accounting separately for measurement and positioning uncertainties as well as considering them both. For each of the three cases, 3000 simulations are performed to statistically characterize results. An almost perfect agreement between imposed motion components $\theta_{r,\text{imp}}$ and mean estimated values $\mu(\theta_r)$ can be observed. Standard deviations vary from 0.122 mm/yr to 0.691 mm/yr for displacements and from 0.006 mrad/yr to 0.066 mrad/yr for rotations. As expected, higher uncertainties are obtained when the contribution of both measurement and positioning uncertainties is accounted for.

Simulations for Case A and Case B are repeated considering different values of imposed displacement or rotation among those listed in Table 1. As an example, trends of the standard deviation and coefficient of variation of the motion parameters with increasing vertical displacement are shown in Fig. 4. It is observed that the measurement uncertainty does not depend on the imposed structural displacement while the positioning uncertainty linearly increases with the vertical displacement. Finally, the total uncertainty is a combination of the measurement and positioning uncertainties. It is worth noting that even if displacements are imposed not for all the five motion parameters, measurement and positioning uncertainties affect the estimation of all motion parameters. This can be observed from Table 2 as well as from Fig. 4(b), where the standard deviation of $\Phi_{y,G}$ with increasing vertical displacement $v_{z,G}$ is analysed. Coefficients of variation of the estimated vertical displacement show values up to about 5% for imposed displacement of 2.5 mm/yr, while they quickly decrease to about 0.5% when $v_{z,G}$ reaches 75 mm/yr.

Further simulations are performed to evaluate the impact of the number of PSs and the measurement and positioning precision on the uncertainty of results. To this purpose, Figs. 5(a) and 5(b) show the trend of $\sigma(v_{z,G})$ for N_S between 14 and 200 (with $n = m = N_S/2$) and for different values of $\overline{\sigma}_M$, namely 0, 1, 2 and 5 mm/yr. Simulations are performed considering the effect of both measurement and positioning uncertainties (Fig. 5(a)) and of the measurement uncertainties only (Fig. 5(b)). In general, the estimated parameter uncertainty decreases when the number of PSs increases and when $\overline{\sigma}_M$ decreases (namely the displacement precision increases). Fig. 6(a) presents the trends of $\sigma(v_{z,G})$ with increasing n and for different values of m, obtained with $\overline{\sigma}_M = 2$ mm/yr and accounting for both measurement and positioning uncertainties. Also in this case it is observed how an increase in the number of PSs implies a reduction of the estimated parameter uncertainty. Finally, Fig. 6(b) shows the trend $\sigma(v_{z,G})$ obtained for

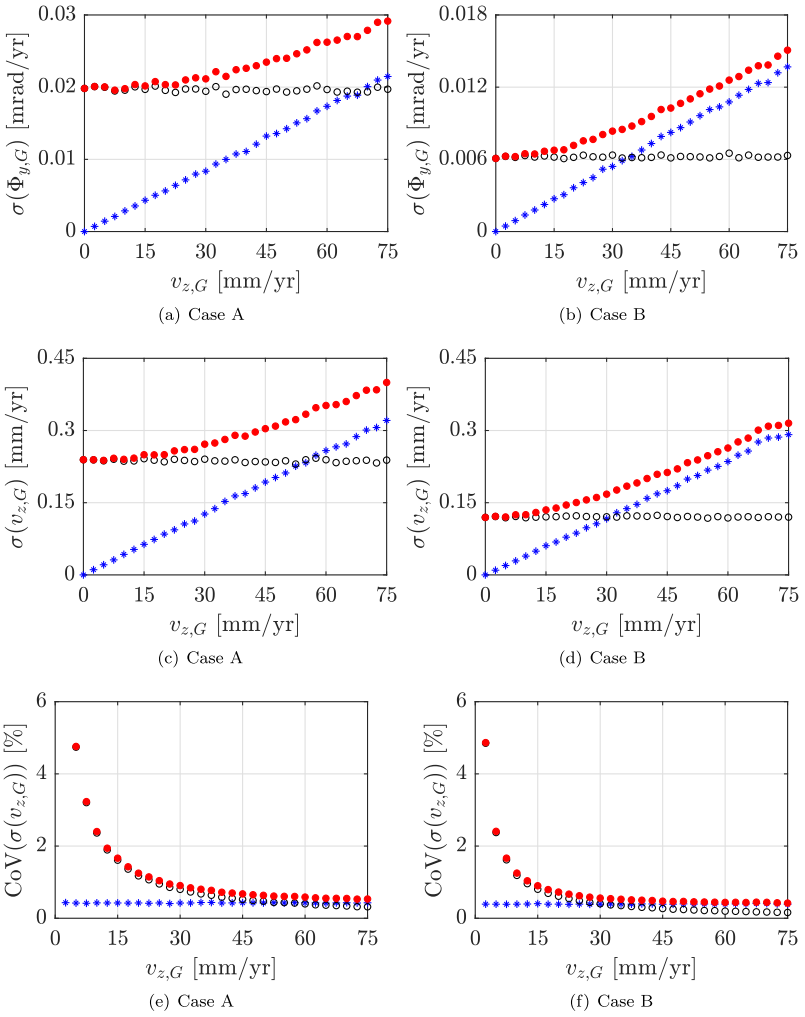

Fig. 4. Trends of (a, b, c, d) standard deviation and (e, f) coefficient of variation with increasing displacement or rotation for Case A (left column) and Case B (right column). Black markers ∘: measuring uncertainties, blue markers ∗: positioning uncertainties, red markers •: measurement and positioning uncertainties. (For interpretation of the references to colour in this figure legend, the reader is referred to the web version of this article.)

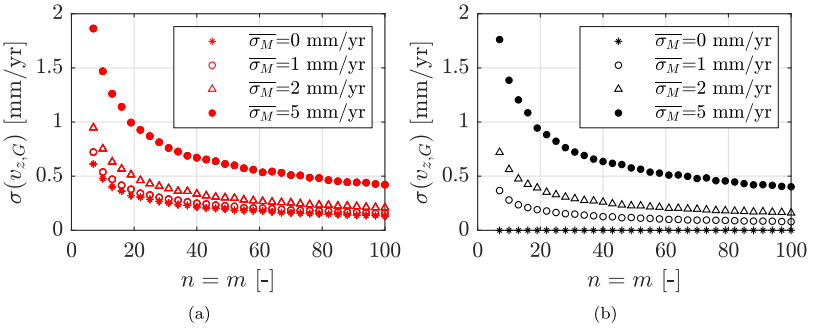

Fig. 5. Case A: Trends of $\sigma(v_{z,G})$ with increasing n for different values of $\overline{\sigma}_M$ obtained considering (a) measurement and positioning uncertainties and (b) measuring uncertainties only. The total number of PSs is $N_S = n + m$ with $n = m$.

different grid cell size considering positioning uncertainties only. As expected, the estimated parameter uncertainty increases with the grid cell size. Note that the maximum number of PSs that can be identified on the structure decreases as the grid cell size increases.

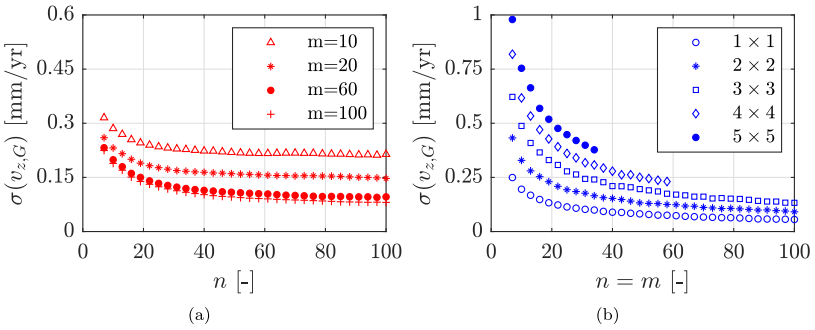

Fig. 6. Case A: Trends of $\sigma(v_{z,G})$ with increasing n for (a) different values of m and (b) for different grid cell size.

Results presented in this section are mainly referred to the vertical displacements $v_{z,G}$. However, similar results are obtained considering also the other motion parameters, which allow drawing the same considerations.

3.4. Main findings

Numerical analyses presented above allowed to evaluate the precision of the rigid motion components estimated from satellite data. Satellite data are simulated considering typical measurement uncertainties (namely $\overline{\sigma}_M = 1$ or 2 mm/yr for COSMO-SkyMed) and positioning uncertainties ($\overline{\sigma}_P = 0.90$ m for COSMO-SkyMed) and the rigid motion parameters are statistically characterized. Simulation results show that the precision in the estimated motion parameters does not depend on the entity of imposed rigid motion displacements if only measurement uncertainties are considered. On the contrary, the standard deviation of the estimated motion parameters linearly increases with the imposed displacements. Finally, as expected, the estimated parameter uncertainties increases with the grill cell size and with $\overline{\sigma}_M$. On the contrary, an increase in the number of PSs leads to a reduction of the estimated parameter uncertainty.

4. Assessment of the motion parameter uncertainty

This section proposes an analytical procedure aimed at assessing the uncertainties of the motion components evaluated from Eq. (9). This is a general procedure that can be applied for every building geometry as long as the hypothesis about the rigid motion is valid. Moreover, the analytical expressions presented in the following apply for PSs with the same height, e.g. in the case of PSs placed on a flat roof, but the procedure can be further generalized to account for different PS heights at the expense of the expression simpleness. The proposed procedure can be adopted in real applications to evaluate the precision by which the motion components can be estimated depending on the number of potentially identified PSs on the analysed structure but before knowing their effective positions. Indeed, some conditions detailed in the following (Eq. (15)) allow removing the dependence of the estimated motion parameter uncertainties on the PS coordinates. Hence, a general expression of the estimated parameter uncertainty depending only on the number of PSs and the building geometry and inclination with respect to the satellite orbits can be formulated.

First, the uncertainty of the estimated rigid motion components is assessed in Section 4.1 and the separate contribution of measurement and positioning uncertainties is analytically defined in Sections 4.2 and 4.3, respectively. Considerations about the uncertainties in the vertical positioning of PSs are discussed in Section 4.4, while the main findings of the analytical procedure are summarized in Section 4.5.

4.1. Problem statement

Starting from Eq. (9) and assuming $(\mathbf{S}^T\mathbf{S})^{-1}\mathbf{S}^T = \mathbf{B}$, the variation of $\boldsymbol{\theta}$ can be expressed using the product rule for derivatives:

$$\Delta\boldsymbol{\theta} = \Delta\mathbf{B}\,\mathbf{M} + \mathbf{B}\,\Delta\mathbf{M} = \sum_h \sum_k \left(\frac{\partial \mathbf{B}}{\partial D_{h,k}}\right)\mathbf{M}\,\Delta D_{h,k} + \mathbf{B}\,\Delta\mathbf{M} \tag{10}$$

where $\mathbf{D}$ is the vector collecting the position of each PS, i.e. $D_{h,k}$. The subscript h represents the direction in which the distance between the PS and G is calculated, with $h = x, y, z$ or $h = x, y$ depending on whether the vertical positioning uncertainty is accounted or not. Subscript k indicates whether the PS is identified from the ascending or the descending orbit, namely $k = i, j$ with $i = 1, ..n$ for the ascending orbit and $j = 1, ..m$ for the descending orbit. Assuming that measurement and positioning uncertainties are independent, i.e. their correlation is zero, the covariance of $\boldsymbol{\theta}$ results:

$$\boldsymbol{\Sigma}(\boldsymbol{\theta}) = \left(\frac{\partial \mathbf{B}}{\partial \mathbf{D}}\mathbf{M}\right)\boldsymbol{\Sigma}(\mathbf{D})\left(\frac{\partial \mathbf{B}}{\partial \mathbf{D}}\mathbf{M}\right)^T + \mathbf{B}\boldsymbol{\Sigma}(\mathbf{M})\mathbf{B}^T \tag{11}$$

where the covariance matrix $\boldsymbol{\Sigma}(\theta)$ provides the covariance between each pair of elements of θ and the main diagonal contains variances. The assumption of independence between measurement and positioning uncertainties is explained as follows. The measurements are derived from the interferometric phases from the stack of images and derived as regression slope of the cumulated displacement with uncertainties of the average displacement arising from the series. Positioning uncertainties are mostly connected to the geometric projection of slant-azimuth plane in the ground range, implying a loose correlation with measurement uncertainties. As a consequence, the correlation between measurement and positioning uncertainties can be considered negligible for structural applications. According to Eq. (11), the covariance matrix $\boldsymbol{\Sigma}(\boldsymbol{\theta})$ can be synthetically expressed as:

$$\boldsymbol{\Sigma}(\boldsymbol{\theta}) = \boldsymbol{\Sigma}_{\mathbf{P}}(\boldsymbol{\theta}) + \boldsymbol{\Sigma}_{\mathbf{M}}(\boldsymbol{\theta}) \tag{12}$$

where $\boldsymbol{\Sigma}_{\mathbf{P}}(\boldsymbol{\theta})$ and $\boldsymbol{\Sigma}_{\mathbf{M}}(\boldsymbol{\theta})$ represent, respectively, the contribution of the positioning and displacement errors to $\boldsymbol{\Sigma}(\boldsymbol{\theta})$. Finally, the total uncertainties of the rth motion component is evaluated from the main diagonal of $\boldsymbol{\Sigma}(\boldsymbol{\theta})$ and reads:

$$\sigma_T(\theta_r) = \sqrt{\sigma_P^2(\theta_r) + \sigma_M^2(\theta_r)} \tag{13}$$

The analytical expressions of $\sigma_M^2(\theta_r)$ and $\sigma_P^2(\theta_r)$ are obtained in the following.

4.2. Measurement uncertainties

As outlined above, the contribution of displacement errors to the covariance matrix $\boldsymbol{\Sigma}(\boldsymbol{\theta})$ is $\mathbf{B}\boldsymbol{\Sigma}(\mathbf{M})\mathbf{B}^T$. Since measurements are assumed as not correlated [25], $\boldsymbol{\Sigma}(\mathbf{M})$ results in a N_S-by-N_S diagonal matrix with diagonal terms equal to $\overline{\sigma}_M^2$. As a consequence:

$$\boldsymbol{\Sigma}_{\boldsymbol{M}}(\boldsymbol{\theta}) = \overline{\sigma}_M^2 \mathbf{B}\mathbf{B}^T = \overline{\sigma}_M^2 (\mathbf{S}^T\mathbf{S})^{-1}\mathbf{S}^T((\mathbf{S}^T\mathbf{S})^{-1}\mathbf{S}^T)^T = \overline{\sigma}_M^2 (\mathbf{S}^T\mathbf{S})^{-1} \tag{14}$$

As stated in Section 3, the displacement precision $\overline{\sigma}_M$ is about 1 or 2 mm/yr when dealing with COSMO-SkyMed data. Being the proposed expressions derived for buildings with flat roof, the height D_z of all the measured PSs is the same, namely $D_{z,i} = D_z$ and $D_{z,j} = D_z$ with $i = 1, \dots, n$ and $j = 1, \dots, m$. To estimate a priori, namely before the effectively identified PSs are known, the variances of the rigid motion components due to measurement uncertainties, it is assumed that the number of PSs measured from the two acquisition geometries is sufficiently high and that they are uniformly distributed over the building roof so that the following conditions apply:

$$\begin{aligned}
&\sum_{i=1}^{n} D_{x,i}^2 = nR_x^2, \ \sum_{j=1}^{m} D_{x,j}^2 = mR_x^2 \\
&\sum_{i=1}^{n} D_{y,i}^2 = nR_y^2, \ \sum_{j=1}^{m} D_{y,j}^2 = mR_y^2 \\
&\sum_{i=1}^{n} D_{x,i} D_{y,i} = nR_{xy}^2, \ \sum_{j=1}^{m} D_{x,j} D_{y,j} = mR_{xy}^2 \\
&\sum_{i=1}^{n} D_{x,i} = 0, \ \sum_{j=1}^{m} D_{x,j} = 0 \\
&\sum_{i=1}^{n} D_{y,i} = 0, \ \sum_{j=1}^{m} D_{y,j} = 0
\end{aligned} \tag{15}$$

where R_x, R_y and R_{xy} are the radius of gyration of the building plan that can be easily evaluated from a geometrical survey. The more PS are identified on the building, the more the conditions in Eq. (15) are true. These assumptions are essential for the definition of a general formulation of the motion parameter uncertainties as they allow to remove the dependence on the PS coordinates.

$\mathbf{S}^T\mathbf{S}$ is a 5-by-5 symmetric matrix whose elements are listed in Appendix. In particular, Eq. (26) presents the matrix elements obtained without applying the conditions in Eq. (15).

Let us now introduce some expressions that will help simplifying the expressions throughout the rest of the paper:

$$\begin{aligned}
f_1 &= n\cos^2\alpha_a + m\cos^2\alpha_a \\
f_2 &= n\sin^2\alpha_a + m\sin^2\alpha_a \\
f_3 &= R_x^2 R_y^2 - R_{xy}^4 \\
f_4 &= \sin\alpha_d \cos\alpha_a + \sin\alpha_a \cos\alpha_d \\
f_5 &= n\cos^4\alpha_a + m\cos^4\alpha_d
\end{aligned} \tag{16}$$

Indicating with $\mathrm{adj}(\mathbf{S}^T\mathbf{S})$ the adjoint of $\mathbf{S}^T\mathbf{S}$, namely the transpose of the cofactor matrix of $\mathbf{S}^T\mathbf{S}$, the inverse of $\mathbf{S}^T\mathbf{S}$ is written:

$$(\mathbf{S}^T\mathbf{S})^{-1} = \frac{1}{|(\mathbf{S}^T\mathbf{S})|}\mathrm{adj}(\mathbf{S}^T\mathbf{S}) \tag{17}$$

where $|(\mathbf{S}^T\mathbf{S})|$ is the determinant of $\mathbf{S}^T\mathbf{S}$ that, assuming the conditions in Eq. (15), reads:

$$|(\mathbf{S}^T\mathbf{S})| = n^2 m^2 R_y^2 f_1 f_3 f_4^4 \tag{18}$$

Once Eq. (14) is solved assuming the conditions in Eq. (15), the variance of each motion parameter related to measurement uncertainties is evaluated from the terms on the main diagonal of $\boldsymbol{\Sigma_M}(\boldsymbol{\theta})$:

$$\begin{aligned}
\sigma_M^2(v_{x,G}) &= \overline{\sigma}_M^2\left(\frac{D_z^2 R_y^2}{f_1 f_3} + \frac{f_1}{nmf_4^2}\right)\\
\sigma_M^2(v_{z,G}) &= \overline{\sigma}_M^2\frac{f_2}{nmf_4^2}\\
\sigma_M^2(\boldsymbol{\Phi}_{x,G}) &= \overline{\sigma}_M^2\left(\frac{f_2}{nmf_4^2 R_y^2} + \frac{R_{xy}^4}{R_y^2 f_1 f_3}\right)\\
\sigma_M^2(\boldsymbol{\Phi}_{y,G}) &= \overline{\sigma}_M^2\frac{R_y^2}{f_1 f_3}\\
\sigma_M^2(\boldsymbol{\Phi}_{z,G}) &= \overline{\sigma}_M^2\frac{f_1}{nmR_y^2 f_4^2}
\end{aligned} \tag{19}$$

According to the results of the numerical simulations presented in Section 3, it is observed that the measurement uncertainties of Eq. (19) do not depend on the structural displacement.

4.3. Positioning uncertainties

The contribution of positioning errors to $\boldsymbol{\Sigma}(\boldsymbol{\theta})$ is represented by the first term of Eqs. (11) and (12):

$$\boldsymbol{\Sigma_P}(\boldsymbol{\theta}) = \left(\frac{\partial \mathbf{B}}{\partial \mathbf{D}}\mathbf{M}\right)\boldsymbol{\Sigma}(\mathbf{D})\left(\frac{\partial \mathbf{B}}{\partial \mathbf{D}}\mathbf{M}\right)^T = \mathbf{J}\boldsymbol{\Sigma}(\mathbf{D})\mathbf{J}^T \tag{20}$$

where $\boldsymbol{\Sigma}(\mathbf{D})$ is a diagonal matrix whose elements are $\overline{\sigma}_{P_x}^2$ and $\overline{\sigma}_{P_y}^2$. Assuming to deal with COSMO-SkyMed data, $\overline{\sigma}_{P_x} = \overline{\sigma}_{P_y}$=0.9 m, leading to $\overline{\sigma}_{P_x}^2 = \overline{\sigma}_{P_y}^2 = 0.81$ m^2. Values of $\overline{\sigma}_P$ for different grid cell size are calculated in Section 3. Note that values of $\overline{\sigma}_P$ presented in Section 3 refer to square grids, implying that $\overline{\sigma}_{P_x} = \overline{\sigma}_{P_y}$. However, the expressions described in the following apply also for $\overline{\sigma}_{P_x} \neq \overline{\sigma}_{P_y}$. In addition, $\mathbf{J}$ is the 5-by-$2(n+m)$ Jacobian matrix that reads:

$$\mathbf{J} = \begin{bmatrix}\mathbf{J}_{x,i} & \mathbf{J}_{y,i} & \mathbf{J}_{x,j} & \mathbf{J}_{y,j}\end{bmatrix} \tag{21}$$

with $i = 1, ..n$ and $j = 1, ..m$. Each block $\mathbf{J}_{h,k}$ that composes the Jacobian matrix is:

$$\mathbf{J}_{h,k} = \frac{\partial \boldsymbol{\theta}}{\partial D_{h,k}} = \begin{bmatrix}\dfrac{\partial v_{x,G}}{\partial D_{h,k}}\\ \dfrac{\partial v_{z,G}}{\partial D_{h,k}}\\ \dfrac{\partial \boldsymbol{\Phi}_{x,G}}{\partial D_{h,k}}\\ \dfrac{\partial \boldsymbol{\Phi}_{y,G}}{\partial D_{h,k}}\\ \dfrac{\partial \boldsymbol{\Phi}_{z,G}}{\partial D_{h,k}}\end{bmatrix} \tag{22}$$

where $h = x, y$ and $k = i, j$. Substituting Eq. (9) into Eq. (22), the formal expression of $\mathbf{J}_{h,k}$ becomes:

$$\begin{aligned}
\mathbf{J}_{h,k} = &\frac{\partial \boldsymbol{\theta}}{\partial D_{h,k}} = \frac{\partial[(\mathbf{S}^T\mathbf{S})^{-1}\mathbf{S}^T]}{\partial D_{h,k}}\mathbf{M} =\\
&\frac{\partial}{\partial D_{h,k}}\left[\frac{1}{|(\mathbf{S}^T\mathbf{S})|}\right]\mathrm{adj}(\mathbf{S}^T\mathbf{S})\mathbf{S}^T\mathbf{M} + \frac{1}{|(\mathbf{S}^T\mathbf{S})|}\frac{\partial[\mathrm{adj}(\mathbf{S}^T\mathbf{S})]}{\partial D_{h,k}}\mathbf{S}^T\mathbf{M} + \frac{1}{|(\mathbf{S}^T\mathbf{S})|}\mathrm{adj}(\mathbf{S}^T\mathbf{S})\frac{\partial \mathbf{S}^T}{\partial D_{h,k}}\mathbf{M} =\\
&\frac{1}{|(\mathbf{S}^T\mathbf{S})|}\left[-\frac{\partial|(\mathbf{S}^T\mathbf{S})|}{\partial D_{h,k}}\mathbf{I} + \frac{\partial[\mathrm{adj}(\mathbf{S}^T\mathbf{S})]}{\partial D_{h,k}}\mathbf{S}^T\mathbf{S} + \mathrm{adj}(\mathbf{S}^T\mathbf{S})\frac{\partial \mathbf{S}^T}{\partial D_{h,k}}\mathbf{S}\right]\boldsymbol{\theta}
\end{aligned} \tag{23}$$

Once the Jacobian matrix is calculated, the variances of each motion parameter relative to positioning uncertainties are evaluated according to Eq. (20). The estimation uncertainty of the rigid motion reads:

$$\mathrm{diag}\left(\boldsymbol{\Sigma_P}(\boldsymbol{\theta})\right) = \begin{bmatrix}\sigma_P^2(v_{x,G})\\ \sigma_P^2(v_{z,G})\\ \sigma_P^2(\boldsymbol{\Phi}_{x,G})\\ \sigma_P^2(\boldsymbol{\Phi}_{y,G})\\ \sigma_P^2(\boldsymbol{\Phi}_{z,G})\end{bmatrix} = \frac{1}{|(\mathbf{S}^T\mathbf{S})|^2}\mathbf{K}\begin{bmatrix}\overline{\sigma}_{P_y}^2\boldsymbol{\Phi}_{x,G}^2 + \overline{\sigma}_{P_x}^2\boldsymbol{\Phi}_{y,G}^2\\ \overline{\sigma}_{P_y}^2\boldsymbol{\Phi}_{z,G}^2\\ \overline{\sigma}_{P_y}^2\boldsymbol{\Phi}_{x,G}\boldsymbol{\Phi}_{z,G}\end{bmatrix} \tag{24}$$

where

$$\mathbf{K} = \begin{bmatrix} K1a & K1b & K1c \\ K2a & K2b & K2c \\ K3a & K3b & K3c \\ K4a & K4b & K4c \\ K5a & K5b & K5c \end{bmatrix} \tag{25}$$

The coefficients of the matrix **K** are listed in Appendix (Eqs. (27)–(31)).

It should be noted that, as expected, the standard deviation of the motion parameters depends only on the rotations $\Phi_{x,G}$, $\Phi_{z,G}$ and $\Phi_{z,G}$ but not on the values of the displacements $v_{x,G}$ and $v_{z,G}$. In other words, an error in the positioning of a PS does not directly produce an error in the evaluation of the vertical or horizontal displacement, if the motion is purely a translation. In this case, the uncertainty in the estimation of the rigid motion parameters due to positioning errors is zero. Conversely, an error in the positioning of a PS produces an uncertainty in the rotation estimate and, therefore, an uncertainty in the displacement estimate since all motion parameters are correlated with each other through Eq. (9).

4.4. Vertical positioning uncertainties

In general, the uncertainties affecting the PSs are related to inaccuracies in the PS displacement measurements and positioning. Positioning uncertainties are related to the position in plan of the PS and to its height. In our approach, the PS height is initially achieved by the interferometric process and, after correcting the PS positioning due to the elevation above terrain, refined using the building height evaluated from a geometrical survey. Hence, the knowledge of the building height makes it possible to neglect the vertical positioning uncertainties. However, the procedure proposed in the manuscript can be generalized to automatically investigate the behaviour of wide urbanized areas, neighbourhoods or districts aiming at monitoring the built heritage on a large scale. In this case, the prior knowledge of the building height from a simple geometrical survey would be unfeasible but the building height could be extracted from a GIS dataset if the numerical cartography is available in the study area. When the building geometry cannot be retrieved with the above mentioned solutions, the scatterer heights should be evaluated through the interferometric technique according to (among the others) [5,27,28]. If so, a further uncertainty contribution related to the uncertainty in the PS height should be added to the positioning uncertainty that has been already discussed.

4.5. Main findings

The analytical expressions derived in Sections 4.2 and 4.3 allow evaluating the uncertainties of the rigid motion parameters estimated from Eq. (9). With the aim of assessing the feasibility of SAR-based structural monitoring, simplifying assumptions are made to evaluate the estimated motion parameter uncertainties a priori, without knowing the actually measured PSs. Motion parameter uncertainties depend on the building height D_z, the building geometry (namely the radius of gyration of the building plan R_x, R_y and R_{xy}) and the number of PSs measured form the ascending (n) and descending (m) orbits. Moreover, motion parameter uncertainties linearly depends on the displacement measurement $\overline{\sigma}_M$ and positioning $\overline{\sigma}_P$ precision. It is also worth noting that, as expected, the measurement uncertainty $\sigma_M(\theta_r)$ does not depend on the structural rigid motion while $\sigma_P(\theta_r)$ depends on the rigid rotations only.

5. Comparison between numerical and analytical results

This section presents a comparison between the rigid motion parameter uncertainties estimated according to the analytical expressions proposed in Section 4.3 and those obtained from the numerical simulations presented in Section 3. The influence of the simplifying conditions on results is investigated in Section 5.1.

Analytical and numerical uncertainties obtained for the previously mentioned Case A and Case B are compared in Table 3 and Fig. 7. Results of Table 3 show a very good match between numerical and analytical standard deviations of the estimated motion parameters. This agreement is confirmed by the comparison presented in Fig. 7.

Fig. 7 shows the linear law modelling the positioning uncertainties, the constant function representing the measurement uncertainties as well as the analytical model for the total uncertainty according to Eq. (13). It can be observed that the analytical expression of σ_M fits very well the corresponding mean values obtained from numerical simulations. Slightly higher differences between numerical and analytical uncertainties are observed for the positioning uncertainties, especially for increasing values of imposed displacement. In particular, when the uncertainty of $\Phi_{y,G}$ with increasing vertical displacement is analysed, the analytical model slightly overestimates the numerical uncertainties. The slight discrepancies observed between the analytical model and the numerical simulations are mainly caused by the simplifying assumptions in Eq. (15).

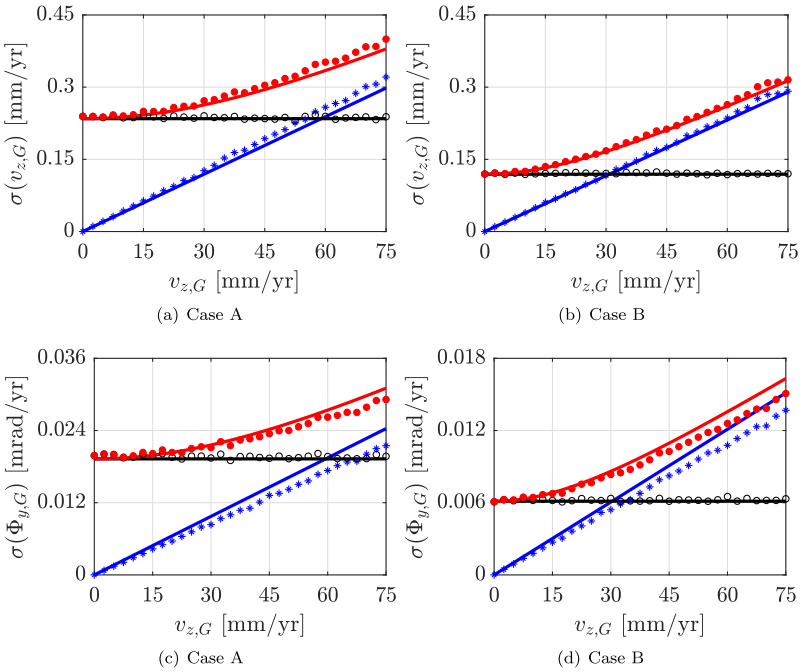

Fig. 7. Comparison between the analytical (bold line) and simulated (markers) trends of (a, b) $\sigma(v_{z,G})$ and (c, d) $\sigma(\Phi_{y,G})$ with increasing vertical displacement for Case A (left column) and Case B (right column). Black bold line and markers ∘: measurement uncertainties $\sigma_M(\theta_r)$, blue bold line and markers ∗: positioning uncertainties $\sigma_P(\theta_r)$, red bold line and markers •: measurement and positioning uncertainties $\sigma_T(\theta_r)$. (For interpretation of the references to colour in this figure legend, the reader is referred to the web version of this article.)

Table 3
Comparison between numerical and analytical standard deviation $\sigma(\theta_r)$ of the motion parameters.

		Case A		Case B	
Measurement unc.		Numerical $\sigma(\theta_r)$	Analytical $\sigma(\theta_r)$	Numerical $\sigma(\theta_r)$	Analytical $\sigma(\theta_r)$
$v_{x,G}$	[mm/yr]	0.538	0.526	0.303	0.299
$v_{z,G}$	[mm/yr]	0.234	0.235	0.122	0.119
$\Phi_{x,G}$	[mrad/yr]	0.028	0.028	0.007	0.007
$\Phi_{y,G}$	[mrad/yr]	0.020	0.019	0.006	0.007
$\Phi_{z,G}$	[mrad/yr]	0.051	0.051	0.014	0.014
Positioning unc.		Numerical $\sigma(\theta_r)$	Analytical $\sigma(\theta_r)$	Numerical $\sigma(\theta_r)$	Analytical $\sigma(\theta_r)$
$v_{x,G}$	[mm/yr]	0.422	0.434	0.484	0.476
$v_{z,G}$	[mm/yr]	0.214	0.195	0.199	0.190
$\Phi_{x,G}$	[mrad/yr]	0.025	0.023	0.011	0.011
$\Phi_{y,G}$	[mrad/yr]	0.014	0.016	0.009	0.010
$\Phi_{z,G}$	[mrad/yr]	0.043	0.042	0.022	0.022
Measurement and positioning unc.		Numerical $\sigma(\theta_r)$	Analytical $\sigma(\theta_r)$	Numerical $\sigma(\theta_r)$	Analytical $\sigma(\theta_r)$
$v_{x,G}$	[mm/yr]	0.691	0.682	0.569	0.562
$v_{z,G}$	[mm/yr]	0.316	0.305	0.233	0.223
$\Phi_{x,G}$	[mrad/yr]	0.037	0.036	0.013	0.013
$\Phi_{y,G}$	[mrad/yr]	0.024	0.025	0.011	0.012
$\Phi_{z,G}$	[mrad/yr]	0.066	0.066	0.026	0.026

5.1. Impact of the simplifying conditions on the analytical uncertainties

This section evaluates the impact of the simplifying conditions in Eq. (15) on the estimated parameter uncertainties. To this purpose, uncertainties $\sigma(\theta_r)$ are evaluated according to the analytical procedure of Section 4.3 without accounting for the conditions in Eq. (15) but considering the effective position of each PS. Values of $\sigma(\theta_r)$ are estimated for N_S varying from 14 to 200 (with $n = m$). For each value of N_S, 3000 values of $\sigma(\theta_r)$ are estimated considering the same PS as the simulations of Section 3. In short, for each simulation of Section 3, the values of $\sum_{i=1}^{n} D_{x,i}^2$, $\sum_{i=1}^{n} D_{x,i}$, etc.. are calculated considering the randomly extracted PS positions. These are then compared to the parameter uncertainties evaluated according to the analytical expressions of Sections 4.2 and 4.3.

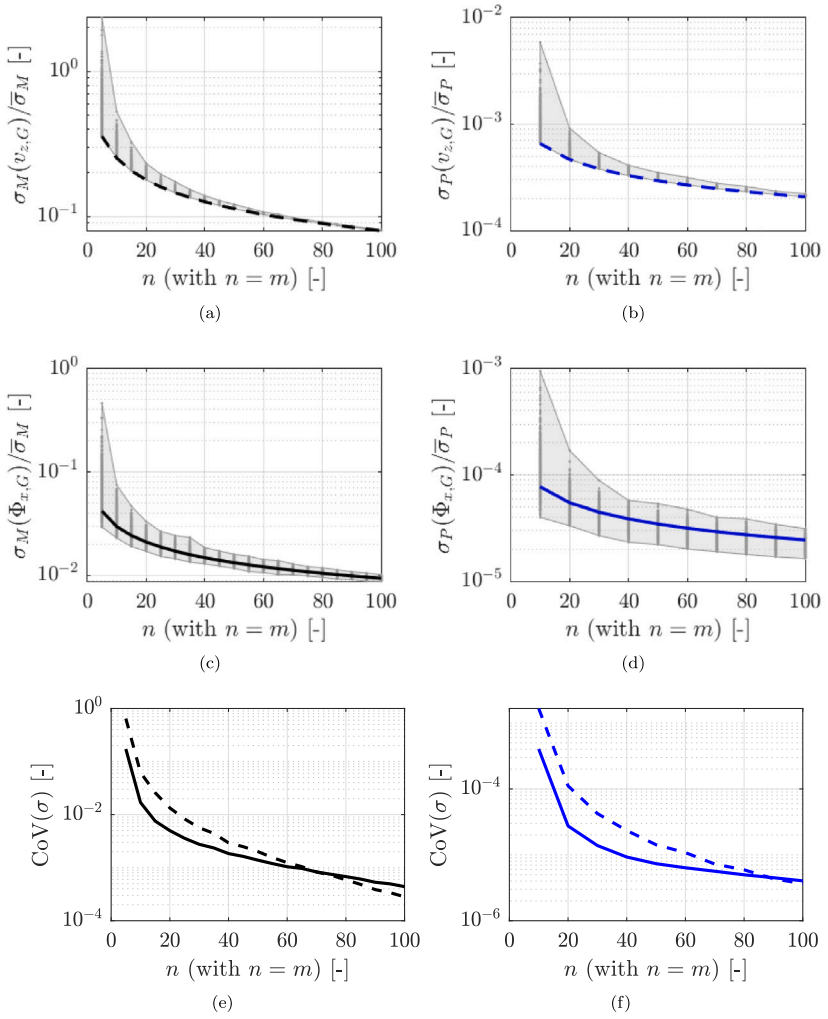

Fig. 8. Case A: trend of (a, b) $\sigma(v_{x,G})$ and (c, d) $\sigma(\boldsymbol{\Phi}_{x,G})$ with n obtained considering (bold lines) or not (grey envelopes) the simplifying conditions. (e,f) Coefficients of variation of $\sigma(v_{x,G})$ (dashed lines) and $\sigma(\boldsymbol{\Phi}_{x,G})$ (continuous lines) evaluated without the simplifying conditions. Left column: measurement uncertainties $\sigma_M(\theta_r)$, right column: positioning uncertainties $\sigma_P(\theta_r)$.

Note that the analytical expressions to evaluate $\sigma(\theta_r)$ without the conditions in Eq. (15) are not presented in the paper but they are freely available on request to the corresponding author.

Figs. 8(a)–8(d) analyse the trend of $\sigma(v_{x,G})$ and $\sigma(\boldsymbol{\Phi}_{x,G})$ with increasing N_S obtained considering the contribution of measurement uncertainties (left column) and positioning uncertainties (right column). The analytical trends of $\sigma(\theta_r)$ (normalized to $\overline{\sigma}_M$ or $\overline{\sigma}_P$) are compared to the envelope of results obtained without the simplifying conditions in Eq. (15). Results show that the uncertainty of $v_{z,\mathrm{G}}$ estimated accounting for the conditions in Eq. (15) corresponds to the lower limit of the envelope of results obtained considering the above mentioned simplifying conditions. On the contrary, analytical trends of $\sigma(\boldsymbol{\Phi}_{x,\mathrm{G}})$ without the simplifying conditions are roughly in between the envelope of $\sigma(\boldsymbol{\Phi}_{x,\mathrm{G}})$ obtained with the simplifying conditions. However, values of $\sigma(v_{x,\mathrm{G}})$ and $\sigma(\boldsymbol{\Phi}_{x,\mathrm{G}})$ calculated without the conditions in Eq. (15) are mainly concentrated close to those obtained considering the above mentioned conditions. This can be observed from Figs. 8(e) and 8(f) that show the coefficients of variation obtained dividing $\sigma(v_{x,\mathrm{G}})$ or $\sigma(\boldsymbol{\Phi}_{x,\mathrm{G}})$ without the simplifying conditions by those obtained according to Sections 4.2 and 4.3. Coefficient of variations present low values that decrease with the number of PSs.

6. Case study

This section presents the application of the proposed procedure to a case study represented by two buildings in Rome (Italy). Fig. 9 highlights the investigated area though a map of the territory and a 3D view. The interferometric processing of satellite data was performed following the workflow based on open-source tools presented in [29] and tailored to COSMO-SkyMed data. In particular,

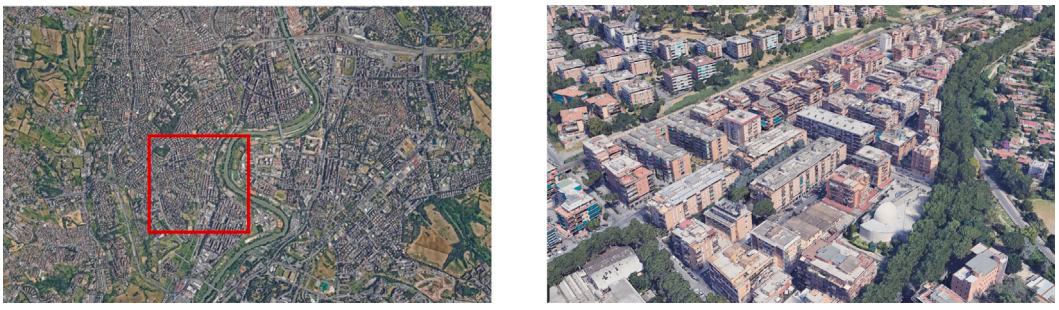

Fig. 9. (a) Map and (b) 3D view of the investigated area in Rome (Italy).

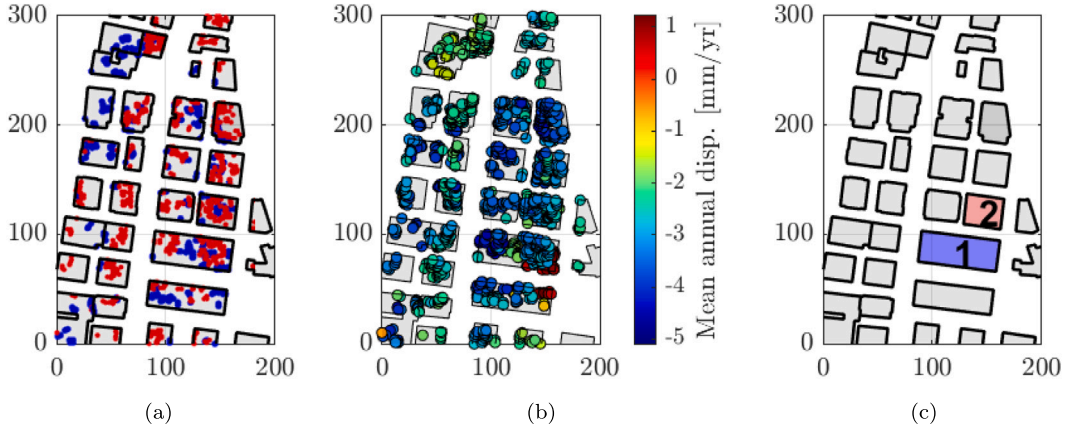

Fig. 10. (a) PSs identified on the buildings from the ascending (blue) and descending (red) satellite acquisition geometry; (b) mean annual displacement of the identified PSs; (c) analysed buildings (1–2). (For interpretation of the references to colour in this figure legend, the reader is referred to the web version of this article.)

a combination of Sentinel Application Platform (SNAP) and Stanford Method for Persistent Scatterers (StaMPS), complemented by a geocoding procedure written by the authors, was adopted. The above mentioned geocoding procedure aims at computing and correcting the planimetric positioning error of the PSs due to their elevation error introduced by inaccuracies of the digital elevation model employed in the interferometric processing. Note that the PS displacement along the LOS is not actually "measured" but it is obtained through PSI from SAR images. Nevertheless, we use "measurement uncertainties" to indicate uncertainties related to the PS displacement along the LOS, for the sake of simplicity. The processed dataset is composed by COSMO-SkyMed Stripmap Himage dual orbit data with a resolution of 3×3 m in range and azimuth. In particular, 135 images for the ascending and 70 images for the descending orbit were processed. The mean incidence angles of the ascending and descending orbits are, respectively, 36.73° and 30.34° and the temporal baseline covers about 8 years for the ascending orbit and almost 7 years for the descending orbit. Persistent scatterers identified on the buildings are presented in Fig. 10(a) while the corresponding mean annual displacements are shown in Fig. 10(b). Analyses presented in the following are referred to the two buildings pointed out in Fig. 10(c), namely Building 1 and 2. Figs. 10(a) and 10(b) display the PSs on the buildings only, which allow for the evaluation of the absolute motion of the analysed buildings. Geometrical characteristics of the analysed buildings and number of identified PSs are listed in Table 4.

Table 5 illustrates the motion components estimated from the PSs on the buildings and the corresponding uncertainties, evaluated accounting or not for the conditions in Eq. (15). The two analysed buildings show a vertical displacement over the investigated period of almost 3 mm/yr and horizontal displacements of about 0.5 mm/yr and 1.3 mm/yr for Building 2 and 1, respectively. Small rotations are observed, which range between −0.0635 mrad/yr and 0.0137 mrad/yr. As expected from the results presented in Fig. 7, the small displacements and rotations affecting the analysed buildings imply that the main contribution to the estimation uncertainties $\sigma_T(\theta_r)$ is given by the measurement uncertainties $\sigma_M(\theta_r)$. Finally, a great agreement between the motion parameter uncertainties evaluated accounting or not for the conditions in Eq. (15) is observed.

Furthermore, the hypothesis of rigid motion is verified as an example for Building 1. To this aim, 30 different subsets composed of 80 randomly selected PSs (40 from the ascending orbit and 40 from the descending orbit) are identified. For each subset, values of the rigid motion components and corresponding uncertainties are estimated. Motion parameter uncertainties are evaluated considering the actual positions of the identified PSs, i.e. without accounting for the conditions in Eq. (15). Mean values and standard deviations

Table 4
Characteristics of the analysed buildings: number of PSs identified form the ascending (n) and descending (m) orbit, building dimensions (L and B) and area (A), radius of gyration of the building plan (R_x, R_y, R_xy) and building height (D_z).

		Building 1	Building 2
n	[–]	59	29
m	[–]	92	65
L	[m]	72.3	34.3
B	[m]	28.3	28.0
A	[m^2]	2045.5	960.7
R_x	[m]	20.7	9.9
R_y	[m]	8.5	8.1
$R_{x,y}$	[m]	0.0	0.0
D_z	[m]	26.7	24.3

Table 5
$\theta_{r,\text{est}}$: rth estimated motion component, $\sigma_M(\theta_r)$, $\sigma_P(\theta_r)$ and $\sigma_T(\theta_r)$: uncertainties in the estimation of the rth motion component obtained accounting for, respectively, measurement uncertainties only, positioning uncertainties only and both measurement and positioning uncertainties. Values of $\sigma(\theta_r)$ are calculated considering the simplifying conditions in Eq. (15) ("Yes") as well as considering the actual positions of the identified PSs ("No").

	Conditions in Eq. (15)	$v_{x,G}$ [mm/yr]	$v_{z,G}$ [mm/yr]	$\Phi_{x,G}$ [mrad/yr]	$\Phi_{y,G}$ [mrad/yr]	$\Phi_{z,G}$ [mrad/yr]
Building 1						
$\theta_{r,\text{est}}$	–	−1.3064	−2.7849	−0.0235	−0.0420	−0.0635
$\sigma_M(\theta_r)$	Yes	0.2129	0.0941	0.0114	0.0046	0.0204
	No	0.2375	0.1118	0.0142	0.0057	0.0233
$\sigma_P(\theta_r)$	Yes	0.0121	0.0046	0.0006	0.0002	0.0010
	No	0.0131	0.0054	0.0007	0.0003	0.0011
$\sigma_T(\theta_r)$	Yes	0.2133	0.0942	0.0115	0.0046	0.0204
	No	0.2379	0.1119	0.0142	0.0057	0.0234
Building 2						
$\theta_{r,\text{est}}$	–	−0.5634	−2.7798	−0.0109	−0.0200	0.0137
$\sigma_M(\theta_r)$	Yes	0.3712	0.1248	0.0154	0.0119	0.0286
	No	0.4469	0.1516	0.0206	0.0141	0.0377
$\sigma_P(\theta_r)$	Yes	0.0059	0.0022	0.0003	0.0002	0.0005
	No	0.0890	0.0026	0.0004	0.0003	0.0007
$\sigma_T(\theta_r)$	Yes	0.3713	0.1248	0.0154	0.0119	0.0286
	No	0.4470	0.1517	0.0206	0.0141	0.0377

of the results obtained from the 30 analyses are reported in Table 6. Mean values of the estimated motion parameters resemble those obtained considering the full set of PSs, standard deviations are of about a smaller order of magnitude, confirming the hypothesis of rigid motion.

The hypothesis of rigid motion is further validated by defining other 17 subsets of PSs as follows rather than randomly. Each subset is composed of the PSs belonging to a specific portion of the building, namely $L_1 \times B$ where B is the smaller building dimension (namely 28.3 m from Table 4) and L_1 varies from 6 m to 56 m with step size 3 m. Fig. 11 shows the trends of the estimated motion parameters for increasing L_1. It can be observed that the estimated motion parameters show great uncertainty when L_1 is lower than about 20 m, i.e. when a very few PSs are considered. On the contrary, estimated motion parameters start to level off for greater values of L_1. In particular, n is less than 6 for $L_1 \leq 24$ m, descending to 2 when $L_1 \leq 12$ m, while several PSs are identified from the descending orbit also for low values of L_1 ($m \geq 19$ for $L_1 \geq 12$ m). It can be observed that the numerosity of PSs for low values of L_1 would be enough, from a numerical point of view, to evaluate the motion parameters. However, a greater number of PSs is required for a reliable estimation of the motion parameters.

7. Conclusions

This paper proposes a procedure for the evaluation of isolated building displacements from satellite SAR measurements. The method allows to assess displacements related to the rigid motion of buildings, generally caused by foundation settlements. In particular, the method focuses on the relative motion of isolated buildings with respect to the surroundings, which may cause damage to structural and non-structural elements. The rigid motion of a building is reconstructed starting from displacements detected by PSI techniques along the line of sight direction. To successfully reconstruct the structural displacement, LOS measurements from dual orbits and high resolution data are required by the model. Due to the limited sensitivity of the SAR measurements to displacement in

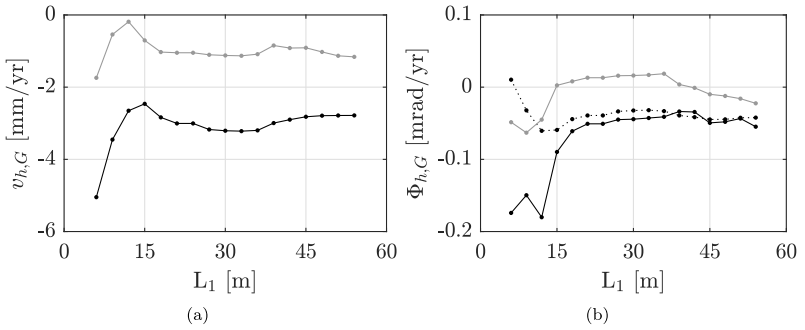

Fig. 11. Trend of (a) $v_{z,G}$ (black), $v_{x,G}$ (grey), (b) $\boldsymbol{\Phi}_{z,G}$ (black), $\boldsymbol{\Phi}_{y,G}$ (dotted) and $\boldsymbol{\Phi}_{x,G}$ (grey) for subsets of PSs identified on different portions of the building roof, namely $L_1 \times B$.

north–south direction, the reconstruction of the original motion vector is limited to components in west–east and vertical directions. The method to reconstruct the building displacements proposed in this paper applies for every isolated building or a portion of it moving like a rigid body.

This paper also proposes an analytical method for quantifying the uncertainties affecting the estimated motion parameters, with the aim to evaluate the reliability of the identified structural motion. The procedure for the evaluation of the 3D rigid motion of buildings and the corresponding uncertainties can be generalized to automatically investigate the behaviour of wide urbanized areas, neighbourhoods or districts aiming at monitoring the built heritage on a large scale. Expressions of the uncertainties presented in this paper are achieved considering the same height for all of the identified PSs, that is the case of buildings with flat roofs. However, the same expressions can be generalized, at the expense of their simpleness, to account for different PS heights. Furthermore, we have assumed that the building height is known from a simple geometrical survey. In case this procedure is automatically applied on a large scale, a geometrical survey is not feasible and the building height can be extracted from a GIS dataset. If the numerical cartography is not available in the study area, the scatterer heights should be evaluated through the interferometric process. In this case, a further uncertainty contribution related to the uncertainty in the PS height should be added to the positioning uncertainty that has been already discussed.

The main benefit of the proposed analytical expressions is that they can be adopted in real applications to a priori evaluate the precision by which the motion parameters can be identified depending only on the number of potentially identified PSs, the building geometry and the satellite orbit inclinations, with no need to know the exact positions of the PSs.

Results presented in the paper allow us to conclude that structural displacements and rotations of the order of some tenths of mm/yr and mrad/yr can be recognized. The precision of the identified displacements or rotations depends on their entity and increases with the PS numerosity. For instance, in the analysed case study the identified rotations are of the order of one hundredth of milliradian and the corresponding uncertainties are of a smaller order of magnitude.

It is important to highlight that the multi-temporal DInSAR-based monitoring can provide insights into the structural behaviour with reference to the past 10–15 years, namely since the recent satellites and constellations suitable for application at building scale were launched. This means that the identification of displacements or rotations below the critical thresholds for buildings does not imply the absence of structural issues, as the contribution of previous displacements or rotations cannot be evaluated. On the contrary, abnormal structural displacements over the recent years can be detected from SAR measurements, allowing for the installation of a specifically designed in-situ monitoring system to investigate the damage evolution.

Declaration of competing interest

The authors declare that they have no known competing financial interests or personal relationships that could have appeared to influence the work reported in this paper.

Data availability

The Matlab file providing the analytical expressions for the evaluation of the rigid motion parameters and the corresponding uncertainties is freely available on request to the corresponding author.

Acknowledgements

The part of this research that concerns the satellite data analysis and the method for the reconstruction of the 3D rigid motion of isolated buildings was supported by the ReLUIS-DPC 2019–2021 Project (Line WP6). The financial support of the Civil Protection Department of the Presidency of the Council of Ministers and the Reluis Consortium is gratefully acknowledged. The research about the estimated motion parameter uncertainties was supported by the FAR Mission Oriented 2021 Project (Satellite Methods for Structural Monitoring, SM4SM). The financial support of the University of Modena and Reggio Emilia, Italy and the "Fondazione di Modena" is also gratefully acknowledged. This work was carried out using COSMO-SkyMed Products by the Italian Space Agency (ASI), delivered under a license to use by ASI.

Table 6
Mean values (μ) and standard deviations (σ) over 30 simulations of the rth estimated motion component ($\theta_{r,\text{est}}$) and the parameter uncertainties obtained accounting for, respectively, measurement uncertainties only ($\sigma_M(\theta_r)$), positioning uncertainties only ($\sigma_P(\theta_r)$) and both measurement and positioning uncertainties ($\sigma_T(\theta_r)$).

		$v_{x,G}$ [mm/yr]	$v_{z,G}$ [mm/yr]	$\Phi_{x,G}$ [mrad/yr]	$\Phi_{y,G}$ [mrad/yr]	$\Phi_{z,G}$ [mrad/yr]
Building 1						
$\theta_{r,\text{est}}$	μ	−1.1906	−2.8077	−0.0190	−0.0466	−0.0647
	σ	0.1134	0.0626	0.0090	0.0026	0.0119
$\sigma_M(\theta_r)$	μ	0.3258	0.1520	0.0198	0.0081	0.0317
	σ	0.0115	0.0047	0.0007	0.0004	0.0011
$\sigma_P(\theta_r)$	μ	0.0158	0.0074	0.0009	0.0005	0.0016
	σ	0.0018	0.0006	0.0001	0.0001	0.0001
$\sigma_T(\theta_r)$	μ	0.3262	0.1522	0.0198	0.0082	0.0317
	σ	0.0115	0.0047	0.0007	0.0004	0.0011

Appendix

In the following, the elements of the matrix $\mathbf{S}^T\mathbf{S}$ are listed.

$$
\begin{aligned}
\mathbf{S}^T\mathbf{S}(1,1) &= n\sin\alpha_a^2 + m\sin^2\alpha_d \\
\mathbf{S}^T\mathbf{S}(1,2) &= -n\sin\alpha_a\cos\alpha_a + m\sin\alpha_d\cos\alpha_d \\
\mathbf{S}^T\mathbf{S}(1,3) &= -\cos\alpha_a\sin\alpha_a\sum_{i=1}^{n} D_{y,i} + \cos\alpha_d\sin\alpha_d\sum_{j=1}^{m} D_{y,j} \\
\mathbf{S}^T\mathbf{S}(1,4) &= (n\sin^2\alpha_a + m\sin^2\alpha_d)D_z + \cos\alpha_a\sin\alpha_a\sum_{i=1}^{n} D_{x,i} - \cos\alpha_d\sin\alpha_d\sum_{j=1}^{m} D_{x,j} \\
\mathbf{S}^T\mathbf{S}(1,5) &= -\sin^2\alpha_a\sum_{i=1}^{n} D_{y,i} - \sin^2\alpha_d\sum_{j=1}^{m} D_{y,j} \\
\mathbf{S}^T\mathbf{S}(2,2) &= n\cos\alpha_a^2 + m\cos^2\alpha_d \\
\mathbf{S}^T\mathbf{S}(2,3) &= \cos^2\alpha_a\sum_{i=1}^{n} D_{y,i} + \cos^2\alpha_d\sum_{j=1}^{m} D_{y,j} \\
\mathbf{S}^T\mathbf{S}(2,4) &= (-n\sin\alpha_a\cos\alpha_a + m\sin\alpha_d\cos\alpha_d)D_z - \cos^2\alpha_a\sum_{i=1}^{n} D_{x,i} - \cos^2\alpha_d\sum_{j=1}^{m} D_{x,j} \\
\mathbf{S}^T\mathbf{S}(2,5) &= \sin\alpha_a\cos\alpha_a\sum_{i=1}^{n} D_{y,i} - \sin\alpha_d\cos\alpha_d\sum_{j=1}^{m} D_{y,j} \\
\mathbf{S}^T\mathbf{S}(3,3) &= \cos^2\alpha_a\sum_{i=1}^{n} D_{y,i}^2 + \cos^2\alpha_d\sum_{j=1}^{m} D_{y,j}^2 \\
\mathbf{S}^T\mathbf{S}(3,4) &= -\cos^2\alpha_a\sum_{i=1}^{n} D_{x,i}D_{y,i} - \cos\alpha_a\sin\alpha_a D_z\sum_{i=1}^{n} D_{y,i} - \cos^2\alpha_d\sum_{j=1}^{m} D_{x,j}D_{y,j} + \cos\alpha_d\sin\alpha_d D_z\sum_{j=1}^{m} D_{y,j} \\
\mathbf{S}^T\mathbf{S}(3,5) &= \sin\alpha_a\cos\alpha_a\sum_{i=1}^{n} D_{y,i}^2 - \sin\alpha_d\cos\alpha_d\sum_{j=1}^{m} D_{y,j}^2 \\
\mathbf{S}^T\mathbf{S}(4,4) &= nD_z^2\sin^2\alpha_a + mD_z^2\sin^2\alpha_d + 2\cos\alpha_a\sin\alpha_a D_z\sum_{i=1}^{n} D_{x,i} + \\
&\quad - 2\cos\alpha_d\sin\alpha_d D_z\sum_{j=1}^{m} D_{x,j} + \cos^2\alpha_a\sum_{i=1}^{n} D_{x,i}^2 + \cos^2\alpha_d\sum_{j=1}^{m} D_{x,j}^2 \\
\mathbf{S}^T\mathbf{S}(4,5) &= -\cos\alpha_a\sin\alpha_a\sum_{i=1}^{n} D_{x,i}D_{y,i} + \cos\alpha_d\sin\alpha_d\sum_{j=1}^{m} D_{x,j}D_{y,j} - D_z(\sin^2\alpha_a\sum_{i=1}^{n} D_{y,i} + \sin^2\alpha_d\sum_{j=1}^{m} D_{y,j}) \\
\mathbf{S}^T\mathbf{S}(5,5) &= \sin^2\alpha_d\sum_{i=1}^{n} D_{y,i}^2 + \sin^2\alpha_a\sum_{j=1}^{m} D_{y,j}^2
\end{aligned}
\tag{26}
$$

where $\mathbf{S}^T\mathbf{S}(h,k)$ is the element in row h column k.

The following Eqs. (27)–(31) present the coefficients of the matrix **K** reported in Eq. (25)

$$
\begin{aligned}
K_{1a} &= m^3 n^3 f_3 f_4^6 R_y^4 (m n f_4^2 f_5 D_z^2 R_y^2 + (m+n) f_1^2 f_3 \cos^2\alpha_a \cos^2\alpha_d) \\
K_{1b} &= m^3 n^3 f_3 f_4^6 R_y^4 (f_1^2 f_3 (m \sin^2\alpha_a \cos^2\alpha_d + n \sin^2\alpha_d \cos^2\alpha_a) + \\
&\quad m n D_z^2 R_y^2 f_4^2 (n \sin^2\alpha_a \cos^2\alpha_a + m \sin^2\alpha_d \cos^2\alpha_d)) \\
K_{1c} &= 2 m^3 n^3 f_3 f_4^6 R_y^4 (m n D_z^2 R_y^2 f_4^2 (n \sin\alpha_a \cos^3\alpha_a + m \sin\alpha_d \cos^3\alpha_d) + \\
&\quad f_1^2 f_3 \cos\alpha_a \cos\alpha_d (m \sin\alpha_a \cos\alpha_d + n \sin\alpha_d \cos\alpha_a))
\end{aligned} \tag{27}
$$

$$
\begin{aligned}
K_{2a} &= m^3 n^3 f_1^2 f_3^2 f_4^6 R_y^4 (m \sin^2\alpha_d \cos^2\alpha_a + n \sin^2\alpha_a \cos^2\alpha_d) \\
K_{2b} &= m^3 n^3 (m+n) f_1^2 f_3^2 f_4^6 R_y^4 \sin^2\alpha_a \sin^2\alpha_d \\
K_{2c} &= 2 m^3 n^3 f_1^2 f_3^2 f_4^6 \sin\alpha_a \sin\alpha_d R_y^4 (m \sin\alpha_d \cos\alpha_a - n \sin\alpha_a \cos\alpha_d);
\end{aligned} \tag{28}
$$

$$
\begin{aligned}
K_{3a} &= m^3 n^3 f_3 f_4^6 R_y^2 (2 m n f_5 R_{xy}^4 \sin\alpha_a \sin\alpha_d \cos\alpha_a \cos\alpha_d + \\
&\quad m \sin^2\alpha_d \cos^2\alpha_a (n^2 R_x^2 R_y^2 \cos^4\alpha_a + 2 m n f_3 \cos^2\alpha_a \cos^2\alpha_d + m \cos^4\alpha_d (m f_3 + n R_{xy}^4)) + \\
&\quad n \sin^2\alpha_a \cos^2\alpha_d (m^2 R_x^2 R_y^2 \cos^4\alpha_d + 2 m n f_3 \cos^2\alpha_a \cos^2\alpha_d + n \cos^4\alpha_a (n f_3 + m R_{xy}^4))) \\
K_{3b} &= m^3 n^3 f_4^6 R_y^2 (2 m n f_3 R_{xy}^4 \sin\alpha_a \sin\alpha_d \cos\alpha_a \cos\alpha_d (n \sin^2\alpha_a \cos^2\alpha_a + m \sin^2\alpha_d \cos^2\alpha_d) + \\
&\quad m n f_3 R_{xy}^4 \cos^2\alpha_a \cos^2\alpha_d (n \sin^4\alpha_a + m \sin^4\alpha_d) + \sin^2\alpha_a \sin^2\alpha_d (m n f_3 f_5 R_x^2 R_y^2 + \\
&\quad f_3^2 (n^3 \cos^4\alpha_a + m^3 \cos^4\alpha_d + 2 m n \cos^2\alpha_a \cos^2\alpha_d (m+n)))) \\
K_{3c} &= 2 m^3 n^3 f_3 f_4^6 R_y^2 (m n R_{xy}^4 \cos^2\alpha_a \cos^2\alpha_d (n \cos\alpha_a \sin^3\alpha_a - m \cos\alpha_d \sin^3\alpha_d) + \\
&\quad n \sin^2\alpha_a \sin\alpha_d \cos\alpha_d (n \cos^4\alpha_a ((2m+n) R_{xy}^4 - n R_x^2 R_y^2) - 2 m n f_3 \cos^2\alpha_a \cos^2\alpha_d - \\
&\quad m^2 R_x^2 R_y^2 \cos^4\alpha_d) - m \sin\alpha_a \sin^2\alpha_d \cos\alpha_a (m \cos^4\alpha_d ((2n+m) R_{xy}^4 - m R_x^2 R_y^2) - \\
&\quad 2 m n f_3 \cos^2\alpha_a \cos^2\alpha_d - n^2 R_x^2 R_y^2 \cos^4\alpha_a))
\end{aligned} \tag{29}
$$

$$
\begin{aligned}
K_{4a} &= m^4 n^4 f_3 f_4^8 f_5 R_y^6 \\
K_{4b} &= m^4 n^4 f_3 f_4^8 R_y^6 (n \sin^2\alpha_a \cos^2\alpha_a + m \sin^2\alpha_d \cos^2\alpha_d) \\
K_{4c} &= 2 m^4 n^4 f_3 f_4^8 R_y^6 (n \sin\alpha_a \cos^3\alpha_a - m \sin\alpha_d \cos^3\alpha_d)
\end{aligned} \tag{30}
$$

$$
\begin{aligned}
K_{5a} &= m^3 n^3 (m+n) f_1^2 f_3^2 f_4^6 R_y^2 \cos^2\alpha_a \cos^2\alpha_d \\
K_{5b} &= m^3 n^3 f_1^2 f_3^2 f_4^6 R_y^2 (n \sin^2\alpha_d \cos^2\alpha_a + m \sin^2\alpha_a \cos^2\alpha_d) \\
K_{5c} &= 2 m^3 n^3 f_1^2 f_3^2 f_4^6 R_y^2 \cos\alpha_a \cos\alpha_d (m \sin\alpha_a \cos\alpha_d - n \sin\alpha_d \cos\alpha_a)
\end{aligned} \tag{31}
$$

References

[1] E. Nochebuena-Mora, N. Mendes, P.B. Lourenço, J.A. Covas, Vibration control systems: A review of their application to historical unreinforced masonry buildings, J. Build. Eng. 44 (2021) 103333, http://dx.doi.org/10.1016/j.jobe.2021.103333, URL https://www.sciencedirect.com/science/article/pii/S2352710221011918.

[2] M. Cheraghzade, M. Roohi, Deep learning for seismic structural monitoring by accounting for mechanics-based model uncertainty, J. Build. Eng. 57 (2022) 104837, http://dx.doi.org/10.1016/j.jobe.2022.104837, URL https://www.sciencedirect.com/science/article/pii/S2352710222008506.

[3] M. Mishra, P.B. Lourenço, G. Ramana, Structural health monitoring of civil engineering structures by using the internet of things: A review, J. Build. Eng. 48 (2022) 103954, http://dx.doi.org/10.1016/j.jobe.2021.103954, URL https://www.sciencedirect.com/science/article/pii/S235271022101812X.

[4] N. Cavalagli, A. Kita, S. Falco, F. Trillo, M. Costantini, F. Ubertini, Satellite radar interferometry and in-situ measurements for static monitoring of historical monuments: The case of Gubbio, Italy, Remote Sens. Environ. 235 (2019) 111453, http://dx.doi.org/10.1016/j.rse.2019.111453, URL https://www.sciencedirect.com/science/article/pii/S0034425719304729.

[5] D. Reale, G. Fornaro, A. Pauciullo, X. Zhu, R. Bamler, Tomographic imaging and monitoring of buildings with very high resolution SAR data, IEEE Geosci. Remote Sens. Lett. 8 (4) (2011) 661–665, http://dx.doi.org/10.1109/LGRS.2010.2098845.

[6] S. Gernhardt, N. Adam, M. Eineder, R. Bamler, Potential of very high resolution SAR for persistent scatterer interferometry in urban areas, Ann. GIS 16 (2) (2010) 103–111, http://dx.doi.org/10.1080/19475683.2010.492126.

[7] F. Casu, M. Manzo, R. Lanari, A quantitative assessment of the SBAS algorithm performance for surface deformation retrieval from DInSAR data, Remote Sens. Environ. 102 (3) (2006) 195–210, http://dx.doi.org/10.1016/j.rse.2006.01.023, URL https://www.sciencedirect.com/science/article/pii/S0034425706000526.

[8] A.K. Gabriel, R.M. Goldstein, H.A. Zebker, Mapping small elevation changes over large areas: Differential radar interferometry, J. Geophys. Res.: Solid Earth 94 (B7) (1989) 9183–9191, http://dx.doi.org/10.1029/JB094iB07p09183, arXiv:https://agupubs.onlinelibrary.wiley.com/doi/pdf/10.1029/JB094iB07p09183, URL https://agupubs.onlinelibrary.wiley.com/doi/abs/10.1029/JB094iB07p09183.

[9] D. Massonnet, M. Rossi, C. Carmona, F. Adragna, G. Peltzer, K. Feigl, T. Rabaute, The displacement field of the landers earthquake mapped by radar interferometry, Nature 364 (1993) 138–142.

[10] P. Rosen, S. Hensley, I. Joughin, F. Li, S. Madsen, E. Rodriguez, R. Goldstein, Synthetic aperture radar interferometry, Proc. IEEE 88 (3) (2000) 333–382, http://dx.doi.org/10.1109/5.838084.

[11] S. Bianchini, F. Pratesi, T. Nolesini, N. Casagli, Building deformation assessment by means of persistent scatterer interferometry analysis on a landslide-affected area: The Volterra (Italy) case study, Remote Sens. 7 (4) (2015) 4678–4701, http://dx.doi.org/10.3390/rs70404678, URL https://www.mdpi.com/2072-4292/7/4/4678.

[12] G. Bru, G. Herrera, R. Tomás, J. Duro, R.D. la Vega, J. Mulas, Control of deformation of buildings affected by subsidence using persistent scatterer interferometry, Struct. Infrastruct. Eng. 9 (2) (2013) 188–200, http://dx.doi.org/10.1080/15732479.2010.519710.

[13] P. Mazzanti, I. Cipriani, Terrestrial SAR interferometry monitoring of a civil building in the city of Rome, in: FRINGE 2011 Work, 2011, pp. 19–23.
[14] M. Del Soldato, L. Solari, F. Poggi, F. Raspini, R. Tomás, R. Fanti, N. Casagli, Landslide-induced damage probability estimation coupling InSAR and field survey data by fragility curves, Remote Sens. 11 (12) (2019) http://dx.doi.org/10.3390/rs11121486, URL https://www.mdpi.com/2072-4292/11/12/1486.
[15] C. Noviello, S. Verde, V. Zamparelli, G. Fornaro, A. Pauciullo, D. Reale, G. Nicodemo, S. Ferlisi, G. Gulla, D. Peduto, Monitoring buildings at landslide risk with SAR: A methodology based on the use of multipass interferometric data, IEEE Geosci. Remote Sens. Mag. 8 (1) (2020) 91–119, http://dx.doi.org/10.1109/MGRS.2019.2963140.
[16] F. Grassi, F. Mancini, E. Bassoli, L. Vincenzi, Contribution of anthropogenic consolidation processes to subsidence phenomena from multi-temporal DInSAR: a GIS-based approach, GIScience Remote Sens. 59 (1) (2022) 1901–1917, http://dx.doi.org/10.1080/15481603.2022.2143683.
[17] S. Gernhardt, R. Bamler, Deformation monitoring of single buildings using meter-resolution SAR data in PSI, ISPRS J. Photogramm. Remote Sens. 73 (2012) 68–79, http://dx.doi.org/10.1016/j.isprsjprs.2012.06.009, Innovative Applications of SAR Interferometry from modern Satellite Sensors, URL https://www.sciencedirect.com/science/article/pii/S0924271612001232.
[18] D.A. Talledo, A. Miano, M. Bonano, F. Di Carlo, R. Lanari, M. Manunta, A. Meda, A. Mele, A. Prota, A. Saetta, A. Stella, Satellite radar interferometry: Potential and limitations for structural assessment and monitoring, J. Build. Eng. 46 (2022) 103756, http://dx.doi.org/10.1016/j.jobe.2021.103756, URL https://www.sciencedirect.com/science/article/pii/S2352710221016144.
[19] F. Di Carlo, A. Miano, I. Giannetti, A. Mele, M. Bonano, R. Lanari, A. Meda, A. Prota, On the integration of multi-temporal synthetic aperture radar interferometry products and historical surveys data for buildings structural monitoring, J. Civ. Struct. Health Monitor. 11 (2021) 1429–1447.
[20] M. Zhu, X. Wan, B. Fei, Z. Qiao, C. Ge, F. Minati, F. Vecchioli, J. Li, M. Costantini, Detection of building and infrastructure instabilities by automatic spatiotemporal analysis of satellite SAR interferometry measurements, Remote Sens. 10 (11) (2018) http://dx.doi.org/10.3390/rs10111816, URL https://www.mdpi.com/2072-4292/10/11/1816.
[21] P. Milillo, G. Giardina, D. Perissin, G. Milillo, A. Coletta, C. Terranova, Pre-collapse space geodetic observations of critical infrastructure: The morandi bridge, genoa, Italy, Remote Sens. 11 (12) (2019) http://dx.doi.org/10.3390/rs11121403, URL https://www.mdpi.com/2072-4292/11/12/1403.
[22] J. Jung, D.-j. Kim, S.K. Palanisamy Vadivel, S.-H. Yun, Long-term deflection monitoring for bridges using X and C-band time-series SAR interferometry, Remote Sens. 11 (11) (2019) http://dx.doi.org/10.3390/rs11111258, URL https://www.mdpi.com/2072-4292/11/11/1258.
[23] A.W. Skempton, D.H. MacDonald, The allowable settlements of buildings, Proc. Inst. Civ. Eng. 5 (6) (1956) 727–768.
[24] G.F. Sowers, in: G.A. Leonards (Ed.), Shallow Foundations, McGraw-Hill Book Co., New York, N.Y., 1962, pp. 525–632.
[25] R.F. Hanssen, Radar Interferometry: Data Interpretation and Error Analysis, in: Remote Sensing and Digital Image Processing, Vol. 2, Springer Dordrecht, 2001, http://dx.doi.org/10.1007/0-306-47633-9.
[26] A. Khuri, J.A. Cornell, Response Surfaces. Designs and Analyses, Marcel Dekker Inc., New York, 1996.
[27] M. Crosetto, O. Monserrat, R. Iglésias, B. Crippa, Persistent scatterer interferometry: Potential, limits and initial C- and X-band comparison, Photogramm. Eng. Remote Sens. 76 (2010) 1061–1069.
[28] M. Rebmeister, A. Schenk, P. Bradley, N. Dörr, S. Hinz, OCLeaS – A tomographic PSI algorithm using orthogonal matching pursuit and complex least squares, Procedia Comput. Sci. 181 (2021) 220–230, http://dx.doi.org/10.1016/j.procs.2021.01.143.
[29] F. Mancini, F. Grassi, N. Cenni, A workflow based on SNAP–StaMPS open-source tools and GNSS data for PSI-based ground deformation using dual-orbit Sentinel-1 data: Accuracy assessment with error propagation analysis, Remote Sens. 13 (4) (2021) 753, http://dx.doi.org/10.3390/rs13040753.
[30] D. Perissin, F. Rocca, High-accuracy urban DEM using permanent scatterers, IEEE Trans. Geosci. Remote Sens. 44 (11) (2006) 3338–3347, http://dx.doi.org/10.1109/TGRS.2006.877754.
[31] M. Yang, P. Dheenathayalan, P. López-Dekker, F. van Leijen, M. Liao, R.F. Hanssen, On the influence of sub-pixel position correction for PS localization accuracy and time series quality, ISPRS J. Photogramm. Remote Sens. 165 (2020) 98–107, http://dx.doi.org/10.1016/j.isprsjprs.2020.04.023, URL https://www.sciencedirect.com/science/article/pii/S0924271620301179.